Biophysical Journal
Article

Biophysical Society

Surface-tethered planar membranes containing the β-barrel assembly machinery: a platform for investigating bacterial outer membrane protein folding

Stephen C. L. Hall,[1] Luke A. Clifton,[1] Pooja Sridhar,[2] David J. Hardy,[2] Peter Wotherspoon,[2] Jack Wright,[4] James Whitehouse,[4] Nadisha Gamage,[5] Claire S. Laxton,[6] Caitlin Hatton,[7] Gareth W. Hughes,[2] Mark Jeeves,[3] and Timothy J. Knowles[2,*]

[1]ISIS Pulsed Neutron and Muon Source, Science and Technology Facilities Council, Rutherford Appleton Laboratory, Oxfordshire, United Kingdom; [2]School of Biosciences, and [3]Institute of Cancer and Genomic Sciences, University of Birmingham, Birmingham, United Kingdom; [4]Astbury Centre for Structural Molecular Biology, University of Leeds, Leeds, United Kingdom; [5]Membrane Protein Laboratory, Diamond Light Source, Harwell Science & Innovation Campus, Oxfordshire, United Kingdom; [6]School of Life Sciences, University of Nottingham, Nottingham, United Kingdom; and [7]School of Life Sciences, University of Warwick, Coventry, United Kingdom

ABSTRACT The outer membrane of Gram-negative bacteria presents a robust physicochemical barrier protecting the cell from both the natural environment and acting as the first line of defense against antimicrobial materials. The proteins situated within the outer membrane are responsible for a range of biological functions including controlling influx and efflux. These outer membrane proteins (OMPs) are ultimately inserted and folded within the membrane by the β-barrel assembly machine (Bam) complex. The precise mechanism by which the Bam complex folds and inserts OMPs remains unclear. Here, we have developed a platform for investigating Bam-mediated OMP insertion. By derivatizing a gold surface with a copper-chelating self-assembled monolayer, we were able to assemble a planar system containing the complete Bam complex reconstituted within a phospholipid bilayer. Structural characterization of this interfacial protein-tethered bilayer by polarized neutron reflectometry revealed distinct regions consistent with known high-resolution models of the Bam complex. Additionally, by monitoring changes of mass associated with OMP insertion by quartz crystal microbalance with dissipation monitoring, we were able to demonstrate the functionality of this system by inserting two diverse OMPs within the membrane, pertactin, and OmpT. This platform has promising application in investigating the mechanism of Bam-mediated OMP insertion, in addition to OMP function and activity within a phospholipid bilayer environment.

SIGNIFICANCE The β-barrel assembly machinery (Bam) complex is responsible for folding and inserting Outer Membrane Proteins (OMPs) into the Gram-negative outer membrane (OM). However, the precise mechanism of Bam-mediated OMP insertion remains uncertain. Here, using established chemistry, we have tethered the complete pentameric Escherichia coli Bam complex to functionalised gold surfaces, prior to reconstitution within a planar phospholipid bilayer. Polarized neutron reflectometry with selective deuteration has revealed colocalization of phospholipids with the transmembrane domain, orientational control over the reconstituted complexes and structures comparable to high-resolution models. Furthermore, we have demonstrated the activity of the reconstituted complex in inserting functional OMPs into the membrane. These data report the development of a robust and powerful platform for investigating Bam-mediated OMP insertion which is compatible with benchtop surface-sensitive techniques.

INTRODUCTION

Gram-negative bacteria contain an extracytoplasmic outer membrane (OM) that is unique in both its constitution and function. Within its makeup there is an asymmetrical assembly of phospholipid on the inner leaflet and lipopolysaccharide on the outer leaflet, with lipoproteins on both sides of the membrane and integral membrane proteins that have a unique β-barrel fold. This organization presents a major topological problem, all components are synthesized in the cytoplasm and must therefore traverse both the inner membrane and the periplasm to reach their site of function. In the case of integral OM β-barrel proteins (OMPs) this is

Submitted February 25, 2021, and accepted for publication October 26, 2021.

*Correspondence: t.j.knowles@bham.ac.uk

Editor: Yuji Sugita.

https://doi.org/10.1016/j.bpj.2021.10.033

achieved by means of translocation in an unfolded form across the inner membrane (IM) via the secretory pathway (SEC) machinery, then ferried across the periplasm in a nonnative but folding-component state via a suite of periplasmic chaperones. At the OM the insertion and assembly of OMPs is mediated by the ubiquitous and essential β-barrel assembly machine (Bam) complex.

How this essential complex functions to fold/insert the myriad OMPs found in the OM is still unclear. OMPs are diverse, with varying numbers of β-strands (8–26 in *Escherichia coli*) and often with the presence of periplasmic/extracellular extramembranous domains. They can be monomeric, consist of small assemblies (dimers, trimers, etc.) or form oligomeric structures (up to 60 stranded pores). They can have varying copy numbers, some low or absent under standard growth (e.g., OmpN (1–4)) conditions, whereas others have in excess of >100,000 copies per cell (e.g., OmpA (1)). Furthermore, the OM is devoid of an energy source, so folding occurs in an apparently energy-independent fashion.

In *E. coli*, the Bam complex is composed of BamA and four lipoproteins BamB, BamC, BamD, and BamE. BamA forms the core of this complex and is an evolutionary conserved OMP with an N-terminal periplasmic domain containing five amino-terminal polypeptide transport associated repeats attached to a C-terminal β-barrel domain embedded in the membrane. Of the four accessory lipoproteins, only BamD is essential in wild-type cells, and is believed to regulate OMP engagement (5) but all are needed for efficient and correct insertion of OMPs into the OM (6).

Current theory postulates four possible models for Bam complex mediated protein folding: 1) the Bam-assisted model, whereby Bam plays a passive role in OMP folding/insertion and functions to target nascent OMPs to a destabilized bilayer produced by its barrel domain (7); 2) the Bam budding model, whereby the nascent OMP barrel grows laterally in to the membrane after templating onto the barrel of BamA (7,8); 3) the swing/elongation model, whereby partial folding/elongation of the OMP occurs in the periplasm on binding to BamA, followed by a conformational change that inserts the folded OMP into the membrane (9,10); and 4) the lumen-catalyzed model, whereby substrates fold against the interior wall of the BamA barrel (11).

From known x-ray crystal structures (12–22), NMR (23–27), small angle x-ray scattering (22,23), and pulsed electron-electron double resonance (PELDOR) (28) spectroscopy, the Bam complex can adopt multiple conformations, both within the barrel, adopting both laterally open and closed conformations, and within the periplasmic region with the polypeptide-associated-transport (POTRA) repeats showing significant conformational flexibility; however, the significance of these are yet to be fully determined, especially because much of this work was performed using either using full or fragments of BamA in isolation or the complex in a detergent background, which does not always reflect accurately the processes occurring within the membrane. Greater understanding of the structural changes that occur and the role the Bam subunits play in folding the diverse array of OMPs into the membrane is therefore a major research goal. Furthermore, increased understanding of Bam-mediated protein folding could lead to the development of novel antibiotics. Indeed, the Bam complex is a significant new target for antimicrobial development as it is essential for membrane biogenesis in Gram-negative pathogens such as *Neisseria meningitidis, Acinetobacter baumannii*, and *Pseudomonas aeruginosa*.

In this study we sought to develop a system that could be used to study Bam complex mediated protein folding at the nanoscale level. Using a combination of quartz crystal microbalance with dissipation monitoring (QCM-D), activity assays and isotopic contrast neutron reflectometry we show tethering of the complete Bam complex to a Cu^{2+}-nitrilotriaceticacid (Cu^{2+}-NTA) derivatized gold surface, bilayer membrane reconstitution and show that the complex is active by monitoring folding of two outer membrane proteins, OmpT, a classical β-barrel protein and pertactin (Ptn), an autotransporter. Precise measurements of the complex within the membrane provide details of the extent the periplasmic domain protrudes within the periplasm, while using specific deuteration we show the position of BamCDE. Together these results provide a basis of an assay system for studying Bam-mediated protein folding at the nanoscale level and provide additional insight into Bam complex mediated protein folding.

MATERIALS AND METHODS

Materials

1-Palmitoyl-2-oleoyl-sn-glycero-3-phosphocholine (POPC) was obtained from Avanti Polar Lipids (Alabaster, AL). All phospholipid samples were used without further purification. Buffer salts and deuterium oxide (D2O) were sourced from Sigma-Aldrich (Gillingham, UK) or Thermo Scientific (Loughborough, UK). n-Dodecyl β-D-maltopyranoside (DDM) and octyl β-D-glucopyranoside (β-OG) were sourced from Anatrace (Maumee, OH, USA) and used without further purification. Silicon crystals (50 × 80 × 20 mm) with a polished 80 × 50-mm face (111 orientation) were obtained from Pi-Kem (Tamworth, UK).

Plasmid construction

Plasmids containing *E. coli* BamAB (pSK38), BamCD (pSK46) were kindly provided by Daniel Kahne. pSK38 was modified slightly to include a 9-residue histidine tag into loop 7 of the BamA barrel between residues Q753-Y754 and termed pSK389H encoding $BamA^{(L7H9)}B$. A plasmid containing *E. coli* BamE was chemically synthesized (Genscript (Leiden, the Netherlands)) lacking sequences corresponding to both the N-terminal signal sequence and cysteine to prevent acylation. This sequence was inserted into pET16b between restriction sites NdeI and XhoI yielding a protein with a Factor Xa cleavable N-terminal deca-histidine tag (Pet-BamE-Nhis).

A plasmid containing *E. coli* SurA (pET-SurA) was chemically synthesized (Genscript), lacking its N-terminal signal sequence, and cloned into

pET28b between restriction sites NdeI and XhoI yielding a protein with a thrombin cleavable N-terminal His-tag. A plasmid containing *E. coli* OmpT (pET-OmpT) was chemically synthesized (Genscript) and cloned in to pET26b between restriction sites NdeI and XhoI to yield the wild-type sequence lacking its N-terminal signal sequence and without a His-tag. A plasmid containing *B. pertussis* Ptn was chemically synthesized (pET-Pert) (Genscript) to lack its N-terminal signal sequence and cloned in to pET21b between restriction sites NdeI and XhoI yielding the WT protein sequence with no purification tag.

Protein production and purification

$BamA^{(L7H9)}$BCDE was expressed from its constituent parts, $BamA^{(L7H9)}$B, BamCD and BamE to allow partial deuteration of the Bam complex yielding the following samples $hBamA^{(L7H9)}$BCDE (fully protonated) and $hBamA^{(L7H9)}$BdCDE (BamCDE deuterated), as detailed in the Supporting materials and methods. Expression and purification of SurA, OmpT and Ptn are detailed in the Supporting materials and methods.

Fluorescence activity assay

Fluorescence activity was based on the method of Iadanza et al. (14). Briefly $BamA^{(L7H9)}$BCDE (5 mg) in DDM was mixed with *E. coli* polar lipid films solubilized in 500 μL TBS, 0.05% (w/v) DDM at a ratio of 2:1 (w/w) lipid/protein and dialyzed extensively against 20 mM Tris (pH 8), 0.01% (w/v) sodium azide at 20°C for 7 days. Resultant proteoliposomes were either flash frozen and stored at −80°C or used for the activity assay. The assay was performed by mixing equal volumes of two subreactions; one containing 1.28 μM $BamA^{(L7H9)}$BCDE proteoliposomes in the presence of 200 μM of the fluoropeptide Abz-Ala-Arg-Arg-Ala-Tyr(NO_2)-NH_2 (peptide synthetics) and the other a mixture of 10 μM OmpT and 30 μM SurA in 20 mM Tris (pH 8), 1.75 M urea. Each subreaction was incubated separately for 15 min before mixing. All OmpT-folding reactions were carried out in 100 μL final volumes. Fluorescence emission was observed following excitation at 325 nm and monitored at 430 nm using a Clariostar fluorometer (BMG Labtech (Aylesbury, UK) with continuous readings for 5 h.

Functionalization of gold surfaces with DTSP-ANTA-Cu^{2+}

Surface modification was based on the method of Hughes et al. (29). Briefly, QCM-D sensors with gold-surface coating (Biolin Scientific, Gothenburg, Sweden) were cleaned by ultraviolet-ozone treatment for 10 min then immersed in a 5:1:1 solution of H_2O/H_2O_2 (25%)/NH_4OH (30%) heated to 75°C for 5 min. The sensors were then rinsed in ultrapure water, dried, and subject to a final ultraviolet-ozone treatment for 10 min. Functionalization was then performed based on the method of Giess to introduce a nitrilotriacetic acid surface (30). Briefly, surfaces were immersed in a solution of 2 mg/mL dithiobis (N-succinimidyl propionate) (DTSP) in anhydrous DMSO for 30 min, then rinsed extensively with anhydrous DMSO, ultrapure water, and ethanol and then dried in a stream of nitrogen. The surfaces were then immersed for 2 h in a solution of 150 mM *N*-(5-amino-1-carboxypentyl) iminodiacetic acid (ANTA) buffered to pH 9.8 with 0.5 M K_2CO_3, then washed with ultrapure water. To charge the surface with Cu^{2+}, 40mM $CuSO_4$ in 50 mM sodium acetate buffer was added and left to incubate for 30 min. The surfaces were then washed with ultrapure water and dried in a stream of nitrogen.

QCM-D

QCM-D was performed using a Q-sense Analyzer QCM-D System (Biolin Scientific, Gothenburg, Sweden). Sensors were mounted into a temperature-controlled flow cell at 20°C attached to a calibrated peristaltic pump and filled with ultrapure H_2O. A flow rate of 0.1 mL/min was used throughout unless otherwise stated. Frequency and dissipation changes (Δf and ΔD) were monitored using multiple harmonics (n = 3, 5, 7, 9, 11, 13) of the resonant frequency. A baseline was acquired for 5 min in H_2O to allow for temperature equilibration before the measurement was started. Buffer was exchanged for β-OG buffer (50 mM Tris (pH 8), 150 mM NaCl, 25 mM β-OG) for 10 min $hBamA^{(L7H9)}$BCDE or $hBamA^{(L7H9)}$BdCDE was diluted to 0.1 mg/mL in the same buffer and injected into the flow cell to bind to the DTSP-ANTA-Cu2 + functionalized surface. Once the Δf_3 (change in frequency of the third harmonic) reached −40 Hz, an arbitrary value chosen for consistency and to limit surface saturation by $BamA^{(L7H9)}$BCDE (e.g., to provide adequate space for lipid coverage), excess $BamA^{(L7H9)}$BCDE was removed by washing with β-OG buffer for 20 min. Mixed POPC and β-OG micelles were prepared by resuspension of a desiccated POPC film in 25 mM β-OG, 20 mM Tris (pH 8), 100 mM NaCl to a concentration of 0.2 mg/mL and subsequent sonication for 30 min to ensure homogeneity. POPC/β-OG mixed micelles were injected into the QCM-D flow cells for 15 min to allow for detergent to exchange for phospholipids. POPC small unilamellar vesicles (SUVs) were prepared by resuspension of a desiccated POPC film in 20 mM Tris (pH 8), 100 mM NaCl to a concentration of 0.2 mg/mL and subsequent sonication for 30 min until an optically transparent solution was obtained. The formation of SUVs of ∼50-nm diameter was confirmed by dynamic light scattering. POPC SUVs were then flowed over the bound $BamA^{(L7H9)}$BCDE for 10 min to deposit a supported bilayer as indicated by the characteristic initial adsorption and subsequent rupture of vesicles indicative of bilayer deposition (31). The surfaces were thoroughly washed for 20 min in 50 mM Tris (pH 8), 150 mM NaCl to ensure excess phospholipids had been removed. To enable Bam-mediated OMP insertion the buffer was exchanged with 20 mM Tris (pH 8), 150 mM NaCl, 20 mM imidazole, 0.8 M urea. Imidazole to prevent nonspecific binding, and urea to prevent aggregation of unfolded OMPs, as used by others in liposome-based assays (14,32). Folding was initiated by the injection of either OmpT or pertactin at a concentration of 0.4 μM in the presence of 4 μM SurA in 20 mM Tris (pH 8), 100mM NaCl, 20 mM imidazole, 0.8 M urea into the cell at a flow rate of 0.1 mL/min. Excess OMP was removed by washing the surfaces in 20 mM Tris (pH 8), 100 mM NaCl, 20 mM imidazole, 0.8 M urea, then into 20 mM Tris (pH 8), 100 mM NaCl, allowing a measured response to be obtained.

Because of the large dissipation shifts observed with QCM-D, the $BamA^{(L7H9)}$BCDE-containing films were not considered rigid. We made the assumption that these films were laterally homogeneous, as supported by our neutron reflectometry analysis, and performed viscoelastic modeling to estimate the mass changes at the surface in response to each analyte. Viscoelastic modeling was performed using Dfind software (Biolin Scientific). Frequency and dissipation values of the 3rd, 5th, 7th, 9th, 11th, and 13th harmonics were modeled using the included "Broadfit" viscoelastic modeling algorithm, with data collected for 20 mM Tris (pH 8), 100 mM NaCl, 25 mM β-OG in the absence of protein and 20 mM Tris (pH 8), 100 mM NaCl, 20 mM imidazole, and 0.8 M urea used as reference value. In line with Reviakine et al. (33) the assumption that the interfacial material is laterally homogeneous with a density similar to that of the bulk solvent, at 1000 g/L was made (33). The density of the bulk solvent was held constant at 1006 g/L, taking into account the density of water at 293 K and buffer components.

In-situ, surface-tethered fluorescence activity assay

$BamA^{(L7H9)}$BCDE was adsorbed onto a DTSP-ANTA-Cu^{2+} functionalized gold QCM-D sensor surface, reconstituted into a POPC bilayer, and interacted with SurA and OmpT as described above. The assembly procedure was monitored using QCM-D to ensure a representative interfacial assembly had been achieved. Control depositions were also conducted, where either $BamA^{(L7H9)}$BCDE was not introduced (resulting in a POPC bilayer which was subsequently interacted with SurA and OmpT), or $BamA^{(L7H9)}$BCDE was fully reconstituted, but not interacted with SurA and

OmpT. Following formation of the interfacial assembly, 100 μM of the fluoropeptide Abz-Ala-Arg-Arg-Ala-Tyr(NO_2)-NH_2 (peptide synthetics) was prepared in 20 mM Tris (pH 8), 100 mM NaCl, and 4 mL independently recirculated over each sensor surface for 24 h in the absence of light. After 24 h, the fluorescence intensity at 430 nm following excitation at 325 nm was measured in sextuplicate using a Fluostar Omega fluorimeter (BMG Labtech). The fluorescence intensity of each sample was normalized to the fluorescence of a sample of the peptide solution that had not been injected into the flow cell. All experiments were performed to n = 3, and significance assessed by means of a one-way ANOVA using GraphPad Prism.

Polarized neutron reflectometry

Polarized neutron reflectometry (PNR) was used to examine the structure across the silicon/water interface. Measurements were undertaken on the POLREF reflectometer at the Rutherford Appleton Laboratory (Oxfordshire, UK). This instrument measures the reflection of white beams of neutrons (34) and is able to operate in a polarized mode; i.e., examine the reflection of a single neutron spin state from a sample surface (which was used for the analysis of the majority of samples discussed here). Polarization was achieved by the use of a polarizing mirror upstream from the sample that selects for a single neutron spin state and a spin flipper which is used to alternate the polarization of the mirror reflected beam. Specular NR measures the neutron reflection as a function of the angle and/or wavelength of the beam relative to the sample (35,36). The reflected intensity was measured as a function of the momentum transfer, Q_z ($Q_z = (4\pi \sin \theta)/\lambda$ where λ is wavelength and θ is the incident angle). The white beam instruments are able probe a wide area of Q_z space at a single angle of reflection because of the use of a broad neutron spectrum. Therefore, to obtain reflectivity data across a Q_z range of ~0.01–0.3 $Å^{-1}$, glancing angles of 0.25,0.5, 1.25, and 2.5° were used with neutron wavelengths of 2–12 Å.

Piranha-acid-cleaned silicon crystal substrates (50 × 80 × 15 mm) with a polished 80 × 50-mm face (111 orientation, surface roughness (RMS) ~3 Å) were ozone-cleaned and sequentially sputter coated with permalloy ($Ni_{80}Fe_{20}$) and gold at the National Institute of Standards and Techniology (NIST) center for Nanoscience and Technology, Gaithersburg, MD, in a Denton Discovery 550 sputtering chamber (Denton Vacuum, Moorestown, NJ, USA)(37,38). Permalloy/gold-coated silicon surfaces were functionalized with DTSP-ANTA-Cu^{2+} using the method described above. These were then placed in solid/liquid flow cells specifically built for the analysis of the solid liquid interface by neutron reflectometry and placed on a variable angle sample stage in the NR instrument (35). The samples are placed in a magnetic field, which orients the magnetic moment of the permalloy layer on the silicon surface, the neutron spin is then manipulated such that it is either parallel or antiparallel to the magnetization of the permalloy layer. The inlet to the liquid cell was connected to a liquid chromatography pump (L7100 HPLC pump; Merck (Gillingham, UK), Hitachi (Tokyo, Japan)), which was used for programmable control change of solution H_2O/D_2O mixtures and solution changes. A flow rate of 1.5 mL/min was used throughout. Bam complex adsorption and reconstitution was performed following the method described for QCM-D experiments above.

Neutron reflectometry data analysis

The magnitude of neutron-scattering length varies randomly across the periodic table (35). Some isotopes, most usefully the hydrogen isotopes protium and deuterium, have different neutron-scattering lengths. The use of differential hydrogen isotope labeling of samples for neutron-scattering experiments is commonly employed to collect a series of sample data sets under chemically similar but isotopically different conditions. Using isotopic labeling of the bulk solution and sample to produce multiple scattering "contrasts" is advantageous when analyzing complex structures, as not only does having multiple data sets greatly limit the number of potential structural solutions to the data when its simultaneously analyzed, but also, if a suitable labeling strategy is employed, the individual distribution of components within the complex can be resolved (35). The SLDs of all components investigated in this study are presented in Table S1.

In addition, the use of a magnetic reference layer in the sample (in the work described here, permalloy (37)) and the collection of reflectivity data using a spin-polarized neutron beam allowed for two distinct reflectivity profiles to be collected (one with spin-up and one for spin-down neutrons) for every isotopic condition examined, which additionally constrained the data fitting.

Neutron reflectivity data were analyzed using the in-house software, RasCal (A. Hughes, ISIS Spallation Neutron Source; Rutherford Appleton Laboratory) that fits layer models describing the interfacial structure calculated using Abelès matrix formalism to the experimental reflectivity data (39). In this approach the interface is described as a series of slabs, each of which is characterized by its SLD, thickness, and roughness. The reflectivity for the model starting point is then calculated and compared with the experimental data. The model parameter values were adjusted using a Simplex fitting algorithm (40) until the model and experimental data sets were in agreement. Complete descriptions of the models used to analyze PNR data are given in the Supporting materials and methods.

Error estimation of the fitted parameters were carried out using RasCal's in-built Bayesian analysis routines (41,42), with the log-likelihood function described in terms of the overall chi-squared. In addition to the model parameters, the backgrounds, scale factors and instrument resolutions were also fitted. Marginalized posteriors were obtained using a Delayed Rejection Adaptive Metropolis algorithm, using 10,000 burn-in iterations, and 100,000 Markov-Chain Monte Carlo (MCMC) iterations, repeated three times. Best fit parameters taken as the distribution maxima, and the uncertainties displayed here were obtained from the shortest 95% confidence intervals of each distribution.

RESULTS AND DISCUSSION

L7 loop modification does not interrupt activity and allows for surface tethering

The particular architecture of the Bam complex negates the possibility of using an N- or C-terminal hexa-histidine tag to orientate the complex correctly onto a surface with its periplasmic face orientated toward the solution as all termini are periplasmic facing. Using separate constructs for BamAB, BamCD, and BamE (32) (required for specific labeling for neutron studies) (kindly provided by Daniel Kahne) we engineered a histidine tag into extracellular loop 7 of BamA. To enhance binding efficiency to planar Cu^{2+}-NTA-functionalized surfaces, an extended His (9) tag was used. $BamA^{(L7H9)}B$, BamCD, and BamE were subsequently expressed and reconstituted as per Hagan et al. (See Supporting materials and methods and Figs. S1–S4) (32). To ensure that this insertion did not overly affect function we tested Bam-mediated OMP folding using an established OmpT-folding assay (14,32) (Fig. 1; Figs. S5 and S6). Clear activity was noted despite the presence of the insert in the L7 loop, suggesting the insertion did not overly affect function.

Fabrication of gold-surface-tethered planar BamABCDE/POPC proteomembrane

Next, a combination of QCM-D and PNR were used to examine the fabrication of a $BamA^{(L7H9)}$BCDE/POPC

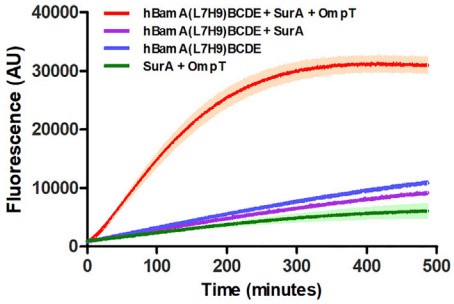

FIGURE 1 Preincubated solutions of urea-denatured OmpT with and without SurA were diluted (at t = 0 min) into liposomes or proteoliposomes containing hBamA$^{(L7H9)}$BCDE. Fluorescence observed following proteolytic cleavage of a self-quenching fluorogenic peptide by OmpT. Data recorded in triplicate with mean and standard deviation (SD) shown.

membrane complex tethered to a DTSP-ANTA-Cu^{2+} self-assembled monolayer functionalized gold surface. Using the approach of Giess et al. (30) the gold surfaces of both quartz crystal microbalance sensor surfaces and gold-coated silicon substrates for PNR were derivatized with a DTSP-ANTA-Cu^{2+} monolayer. Cu^{2+} was chosen over Ni^{2+} due to its higher affinity for polyhistidine tags. Fig. 2 *a* depicts a schematic of the assembly process followed throughout this study. Initially BamA$^{(L7H9)}$BCDE, solubilized in β-OG micelles is adsorbed to the DTSP-ANTA-Cu^{2+} functionalized gold surface. Reconstitution is initiated by exchanging β-OG for mixed micelles of β-OG and phospholipids. Finally, phospholipid SUVs are introduced, leading to vesicle adsorption, fusion and ultimately rupture, resulting in a planar phospholipid bilayer containing BamA$^{(L7H9)}$BCDE.

QCM-D was used to follow the assembly process in real-time through mass changes on the sensor surface while PNR utilizing an isotopic and magnetic-contrast variation approach (35) was used to structurally resolve changes in the relative distribution of SAM, protein, lipid, and water in the interfacial assembly.

QCM-D measurements (Fig. 2 *b*) showed that following equilibration of the flow cells in β-OG containing buffer (Fig. 2 *b*, *i*), subsequent injection of BamA$^{(L7H9)}$BCDE solubilized within β-OG micelles (Fig. 2 *b*, *ii*) leads to a large decrease in resonant frequency and a concomitant increase in dissipation, indicative of the adsorption of viscoelastic material onto the surface. Removal of excess BamA$^{(L7H9)}$BCDE/β-OG micelles by continuous flushing with β-OG containing buffer (Fig. 2 *b, iii*) leads to a small increase in frequency, and a decrease in dissipation suggesting the removal of nonspecific, weakly adsorbed species from the surface, resulting in a more rigid monolayer of BamA$^{(L7H9)}$BCDE adsorbed to the surface. Reconstitution of a PL bilayer around the complex was then achieved using the approach of Tiberg et al. (43), based on the higher aqueous solubility of the detergent with respect to the lipid.

POPC was chosen for the lipid due to the mixed saturation of the acyl chains, thermotropic properties and zwitterionic headgroup providing an ideal balance between a realistic structural analog of the *E. coli* OM, and amenability for formation of supported lipid bilayers on protein functionalized surfaces, even though it is not a constituent of *E. coli* membrane (29,44,45). Here, a buffer containing POPC in β-octylglucoside at a molar ratio of 1:10 was injected. A slight decrease in the frequency with constant dissipation was observed (Fig. 2 *b, iv*) which is consistent with others, and is detergent dependent (46). We next injected pure POPC SUVs alone resulting in a dramatic decrease in frequency and a concomitant increase in dissipation followed rapidly by desorption and stabilization. This behavior is characteristic of vesicular adsorption, leading to a large increase in adsorbed mass, until a critical lipid surface excess is reached, leading to vesicle fusion and rupture, resulting in a decrease in mass (and increase in frequency) and a more rigid film constrained by a lipid bilayer (as indicated by a decrease in dissipation). The resulting stabilized signal following washing to remove excess POPC (Fig. 2 *b, vi*) showed similar values of frequency and dissipation to the presence of adsorbed BamA$^{(L7H9)}$BCDE/β-OG alone and is presumably because of the restructuring of the environment around the protein resulting in removal of β-OG and its replacement with a continuous bilayer of POPC and stabilizing BamA$^{(L7H9)}$BCDE, consistent with our previous findings (29).

For PNR measurements, the silicon substrates were sequentially coated with layers of permalloy (a nickel and iron alloy) and gold. The magnetized permalloy underlayer allowed an approach to be employed where NR was collected with differing polarizations of the neutron beam, being either parallel (spin up ($\uparrow$)) or antiparallel (spin down ($\downarrow$)) to that of the permalloy. This meant that for each individual solution isotopic contrast collected, two distinct data sets were obtained which differed only in the SLD of the permalloy layer (which is a combination of nuclear and magnetic scattering) but not the gold/water interface, which was of interest, where the SLD is dependent only on the isotopic contribution of the interface. This approach has been shown to allow for additional precision in the resolution of complex interfacial architectures like the proteolipid complexes reported here (47).

Details on the assembly and structure of hBamA$^{(L7H9)}$BCDE/POPC complex was examined with PNR to provide precise details on the relative distributions of the SAM, lipid and protein components of the interfacial assemblage and therefore validate the model membrane system and ascertain whether within the confines of a phospholipid bilayer the Bam complex adopts a conformation consistent with published detergent solubilized crystal structures (12,14–16). NR is uniquely suited to study membrane protein architecture within or on a lipid bilayer and is able to provide information that is not available by other

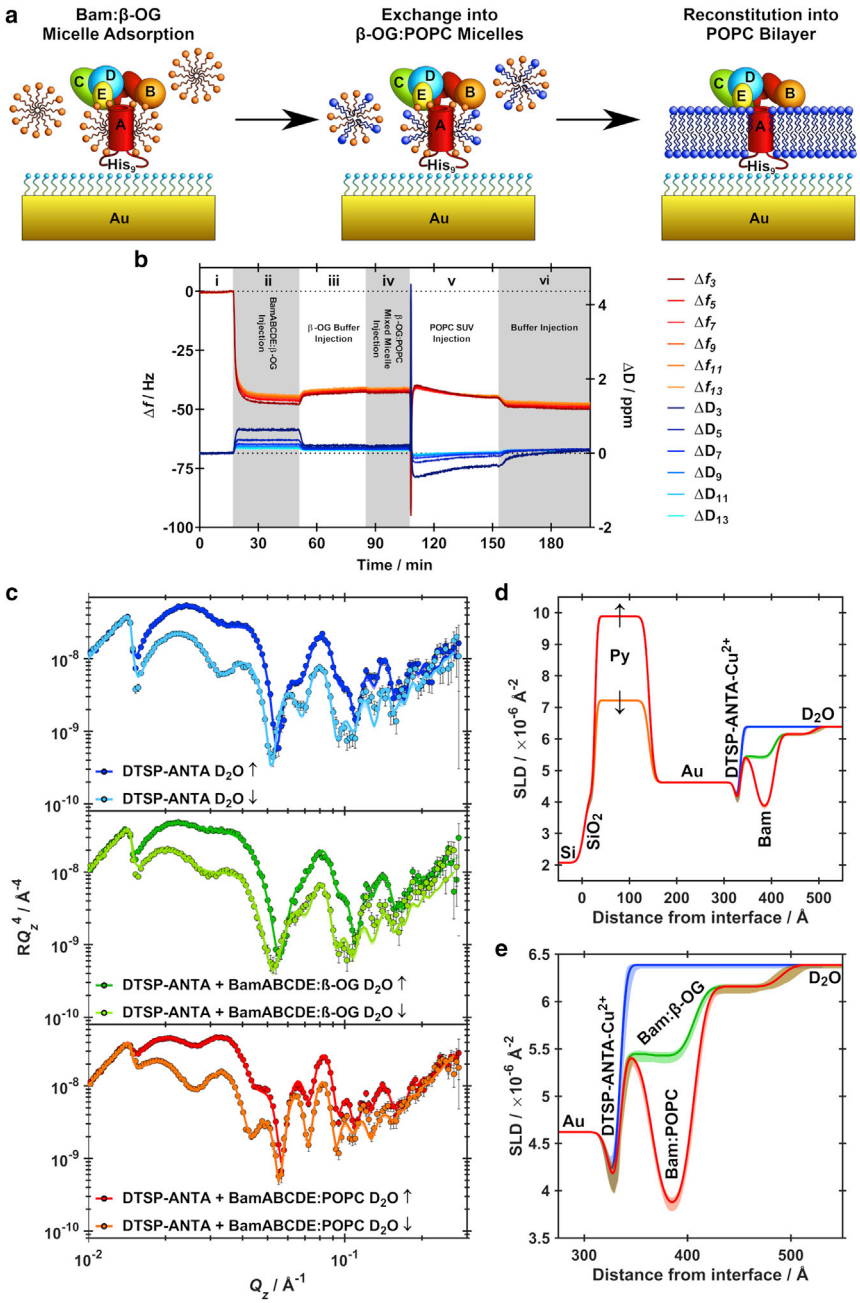

FIGURE 2 (*a*) Schematic detailing the assembly process of surface-tethered BamA$^{(L7H9)}$BCDE/POPC sensor surfaces. (*b*) QCM-D data following the assembly procedure. (*c*) PNR data (*points*) and fits (*lines*) corresponding to D_2O solution contrast with both spin-up (↑) and spin-down (↓) magnetic contrasts for the functionalized gold substrates before hBamA$^{(L7H9)}$BCDE adsorption (*blue*), after the adsorption of hBamA$^{(L7H9)}$BCDE within *β*-OG micelles (*green*) and upon reconstitution of hBamA$^{(L7H9)}$BCDE within a POPC bilayer (*blue*). (*d*) SLD profiles of the complete interface throughout the assembly process of a hBamA$^{(L7H9)}$BCDE/POPC proteomembrane, derived from fits to NR data shown in (*c* and *e*). SLD profile of the functionalized gold/water interface derived from fits shown in (*c*). Shaded regions represent 95% confidence intervals determined from MCMC resampling of the experimental data fits.

techniques. The protein position and distribution profile normal to the membrane surface as well as bilayer thickness upon protein binding can be measured with precision on the ångström scale (35,48).

Results showed the addition of hBamA$^{(L7H9)}$BCDE stabilized with *β*-OG was coincident with changes in the PNR data (Fig. 2 *c*), which revealed a layer of protein depositing adjacent to the DTSP-ANTA-Cu^{2+} self-assembled monlayer (SAM) surface. This protein layer consisted of a dense region close to the functionalized gold surface and a more diffuse region next to the bulk solution (Fig. 2, *d* and *e*).

Once it was confirmed that protein had deposited onto the gold/water interface POPC was added to the sample over an increasing gradient of POPC and decreasing *β*-OG until only POPC was present, followed by the removal of excess lipid (similar to that conducted for QCM measurements). The structure at the gold/water interface was again examined and the structure adjacent to the DTSP-ANTA-Cu^{2+} SAM was now found to have changed significantly following the interaction of the vesicles with the surface adhered Bam complex (Fig. 2).

The hBamA$^{(L7H9)}$BCDE/POPC membrane was characterized in four solution contrasts: D_2O, gold-matched water

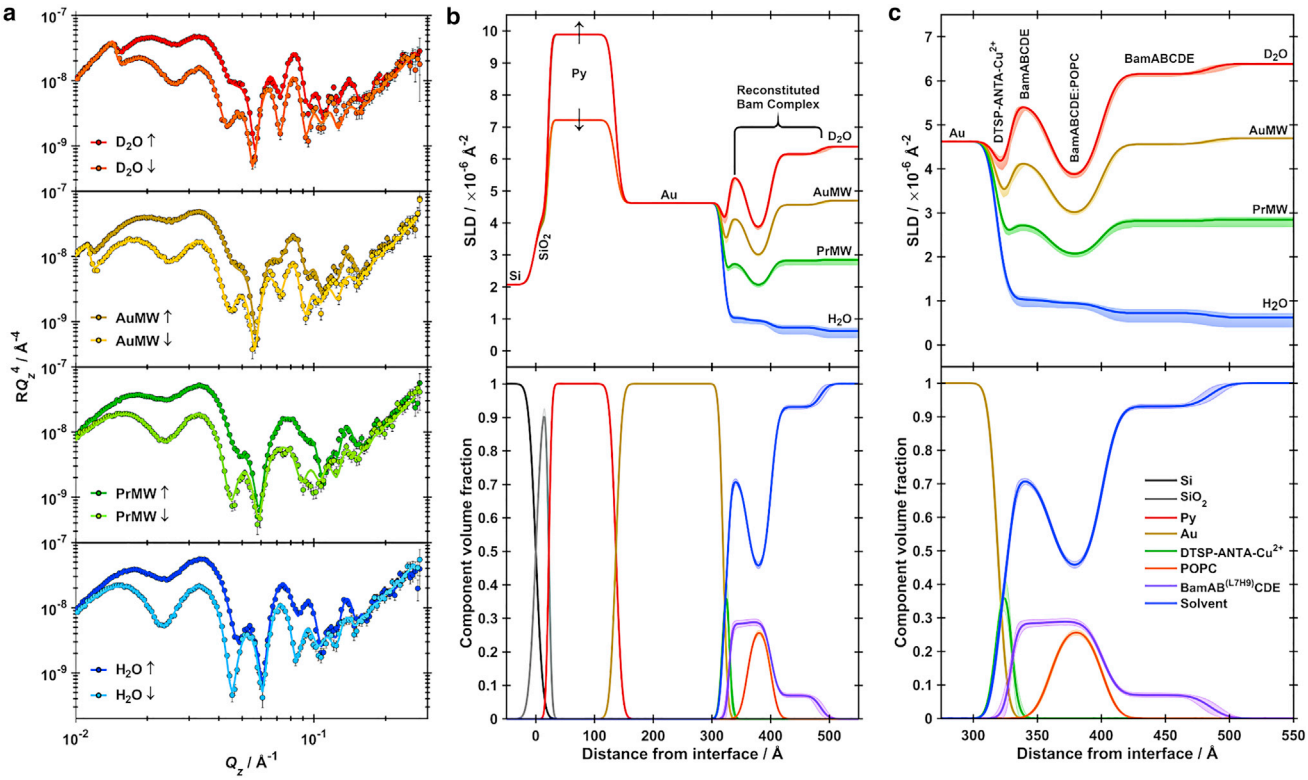

FIGURE 3 (*a*) PNR data (*points*) and fits (*lines*) for a hBamA$^{(L7H9)}$BCDE/POPC membrane adsorbed to a DTSP-ANTA-Cu^{2+} functionalized gold surface, characterized in both spin-up (↑) and spin-down (↓) magnetic contrasts in D_2O (*red data*), Gold-matched water (*gold data*), PrMW (*green data*) and H_2O (*blue data*) solution isotopic contrasts. SLD profiles (*top* panels) and component volume fraction profiles (*bottom* panels) corresponding to fits shown in (*a*), describing (*b*), the complete interfacial structure and (*c*), the membrane-containing region. Shaded regions represent the 95% confidence intervals determined from MCMC resampling of fits to the experimental data.

(AuMW; 75% D_2O, 25% H_2O), protein-matched water (PrMW; 36% D_2O, 64% H_2O) and H_2O (Fig. 3 *a*). Models fit to these data, found the structure of the hBamA$^{(L7H9)}$BCDE/POPC membrane to contain three distinct regions (Fig. 3, *b* and *c*). These regions were identified, moving from the gold surface to the bulk solution, as a protein only layer adjacent to the gold bound NTA SAM, a composite protein-lipid bilayer region and a protein only peripheral membrane region facing the extracellular solution. Table 1 lists structural parameters obtained from the fitting of the experimental reflectivity data.

The proteinaceous region closest to the DTSP-ANTA-Cu^{2+} SAM was found to be ∼3 nm in thickness and presumably partially composed of the nona-histidine tag binding the BamA$^{(L7H9)}$BCDE to the NTA SAM surface as well as surface exposed extracellular loops of BamA. Adjacent to this away from the gold surface is a lipid bilayer region of the membrane which consists of 26^{+1}_{-1} % POPC, 29^{+1}_{-1} % embedded Bam protein chain and 45^{+1}_{-1}% hydration from the bulk solvent.

The hydration within the lipid bilayer region of the structure is likely to be due to three factors. Firstly, defects in the bilayer due to patches across the surface which do not contain the membrane structure (49). Secondly, there is a possibility that residual β-OG remains associated with the membrane, resulting in an increase in hydration. Given the low volume fraction of interfacial β-OG present before reconstitution, and the subsequent dilution below the CMC, we anticipate this factor to be negligible, though without measurements with deuterated surfactant, is challenging to unequivocally rule out. Finally, in a composite protein-lipid bilayer the protein will have inherent hydration. In the neutron-scattering data analysis conducted here the volume fraction of protein refers to the chain only, i.e., no hydration is accounted for. Protein crystals are known to contain 30% or more hydration, exemplifying the importance of hydration in maintaining protein structure (50). Recently, when examining the binding of the antibacterial protein colicin-N to a membrane surface, MD simulations of the protein suggested that the volume fraction of ∼40% protein chains was equivalent to a complete coverage of the protein on a membrane surface due to intrinsic protein hydration (51). Here, the membrane embedded region of the protein complex is likely to be predominantly composed of BamA (16). Volume fractions of the protein chain embedded in the membrane and the solution component are similar at ∼29 and ∼45%, respectively.

TABLE 1 Structural parameters obtained by fitting PNR data of hBamA$^{(L7H9)}$BCDE/POPC membrane tethered to an Si-Py-Au-DTSP-ANTA-Cu^{2+} substrate

Layer	Thickness (Å)	Net SLD ($\times 10^{-6}$ Å^{-2})		Component volume fractions (%)		Roughness (Å)
Si	ND		2.07[a]	Si:	100[a]	$9.6^{+0.3}_{-0.6}$
SiO_2	$22.2^{+0.6}_{-0.5}$		$4.41^{+0.08}_{-0.12}$	SiO_2:	100[a]	$4.1^{+0.5}_{-0.5}$
Permalloy	$114.3^{+0.3}_{-0.2}$	↑:	$9.89^{+0.01}_{-0.01}$	Permalloy:	100[a]	$8.3^{+0.3}_{-0.3}$
		↓:	$7.22^{+0.01}_{-0.01}$			
Gold	$182.7^{+0.4}_{-0.3}$		4.62[a]	Gold:	100[a]	$5.9^{+0.1}_{-0.1}$
DTSP-ANTA-Cu^{2+} SAM	$9.8^{+1.3}_{-1.4}$		1.80[a]	DTSP-ANTA-Cu^{2+}:	56^{+8}_{-6}[b]	$4.6^{+1.7}_{-2.0}$
				Solvent:	44^{+6}_{-8}	
hBamA$^{(L7H9)}$BCDE (between SAM and membrane)	$31.2^{+1.6}_{-1.6}$	D_2O:	$3.08^{+2.17E-3}_{-2.93E-3}$[b]	hBamA$^{(L7H9)}$BCDE:	28^{+1}_{-1}[b]	$9.8^{+0.2}_{-0.3}$
		AuMW:	$2.78^{+0.43E-3}_{-0.58E-3}$[b]			
		PrMW:	$2.45^{+0.01}_{-0.01}$[b]	Solvent:	72^{+1}_{-1}	
		H_2O:	$2.05^{+0.05}_{-0.02}$[b]			
hBamA$^{(L7H9)}$BCDE + β-OG	$40.6^{+1.6}_{-1.7}$	D_2O:	$3.07^{+0.01}_{-0.02}$[b]	β-OG:	$0.2^{+0.3}_{-0.2}$	$9.8^{+0.2}_{-0.3}$
				hBamA$^{(L7H9)}$BCDE:	29^{+1}_{-1}[b]	
				Solvent:	71^{+1}_{-1}[b]	
hBamA$^{(L7H9)}$BCDE + POPC bilayer	$40.6^{+1.6}_{-1.7}$	D_2O:	$1.74^{+0.04}_{-0.04}$[b]	POPC:	26^{+1}_{-1}[b]	$9.8^{+0.2}_{-0.3}$
		AuMW:	$1.58^{+0.04}_{-0.03}$[b]	hBamA$^{(L7H9)}$BCDE:	29^{+1}_{-1}[b]	
		PrMW:	$1.41^{+0.03}_{-0.03}$[b]	Solvent:	45^{+1}_{-1}	
		H_2O:	$1.20^{+0.03}_{-0.03}$[b]			
hBamA$^{(L7H9)}$BCDE (adjacent to bulk solvent)	$84.4^{+7.1}_{-8.0}$	D_2O:	$3.08^{+2.17E-3}_{-2.93E-3}$[b]	hBamA$^{(L7H9)}$BCDE:	7^{+1}_{-1}[b]	$9.8^{+0.2}_{-0.3}$
		AuMW:	$2.78^{+0.43E-3}_{-0.58E-3}$[b]	Solvent:	93^{+1}_{-1}	
		PrMW:	$2.45^{+0.01}_{-0.01}$[b]			
		H_2O:	$2.05^{+0.02}_{-0.02}$[b]			
Bulk solvent	ND	D_2O:	$6.39^{+0.01}_{-0.02}$	Solvent:	100[a]	ND
		AuMW:	$4.70^{+2.39E-3}_{-3.25E-3}$			
		PrMW:	$2.84^{+0.06}_{-0.06}$			
		H_2O:	$0.62^{+0.10}_{-0.09}$			

Error values indicate the 95% confidence intervals estimated from MCMC resampling.
ND, not determinable.
[a]Values were held constant throughout the fitting procedure.
[b]Values were not directly fit, but calculated from the fitted parameters and associated 95% confidence intervals calculated from MCMC chains of the dependent fitted parameters.

Using the ability of the Bam complex to be formed from its component parts, BamAB, BamCD and BamE and the fact that the nuclear neutron-scattering length varies greatly between the isotopes of hydrogen: protium (^{1}H) and deuterium (^{2}H), with there being a greater coherent scattering cross section for ^{2}H, deuteration of BamCDE could lead to enhanced contrast relative to BamAB and the lipid bilayer to more firmly identify the location of these components within the membrane environment. Complex deposition was performed in a similar manner and the structure of the solid/liquid interface was again examined using PNR (Fig. 4 *a*). The architecture of the hBamA$^{(L7H9)}$B dCDE/POPC membrane (Fig. 4, *b* and *c*) was consistent with that of hBamA$^{(L7H9)}$BCDE, demonstrating the robustness of the assembly procedure. Three distinct regions of similar thicknesses were again revealed, with a protein only layer adjacent to the gold bound Cu^{2+}-NTA SAM, a composite protein-lipid bilayer region and a protein only peripheral membrane region facing the extracellular solution. The complexity of the interfacial assembly meant that absolute confirmation of the position of the deuterated (dBamCDE) component was challenging. However, with the inclusion of a natural abundance hydrogenated protein contrast matched water data set (PrMW) data suggested, at least, a partial presence of the deuterated component in the region of protein distribution outside the hydrophobic core of the membrane, adjacent to bulk solvent (Fig. 4 *c*; Table 2). This is consistent with the expected structure of the assembled Bam complex from high-resolution structures determined to date (12,14–16), where the periplasmic peripheral region is composed of POTRA domains of BamA, and BamB (which in this case will be hydrogenated) complexed with BamCDE (which are deuterated in this case). Similarly, the observed thicknesses of both the transmembrane and peripheral regions are consistent with known high-resolution structures (Fig. 4 *c*).

Recent studies have used a similar approach using a Ni^{2+} chelating SAM on a gold support to investigate the structure of BamA (52). Compared with these data, the complete reconstituted Bam complex investigated here shows a notable compaction of the peripheral membrane region corresponding to the POTRA domains. Presumably, this is due to conformational restrictions imparted on the complex though intersubunit interactions. This observation highlights the importance of reconstituting the complete Bam complex to ensure the adoption of a physiologically relevant conformation.

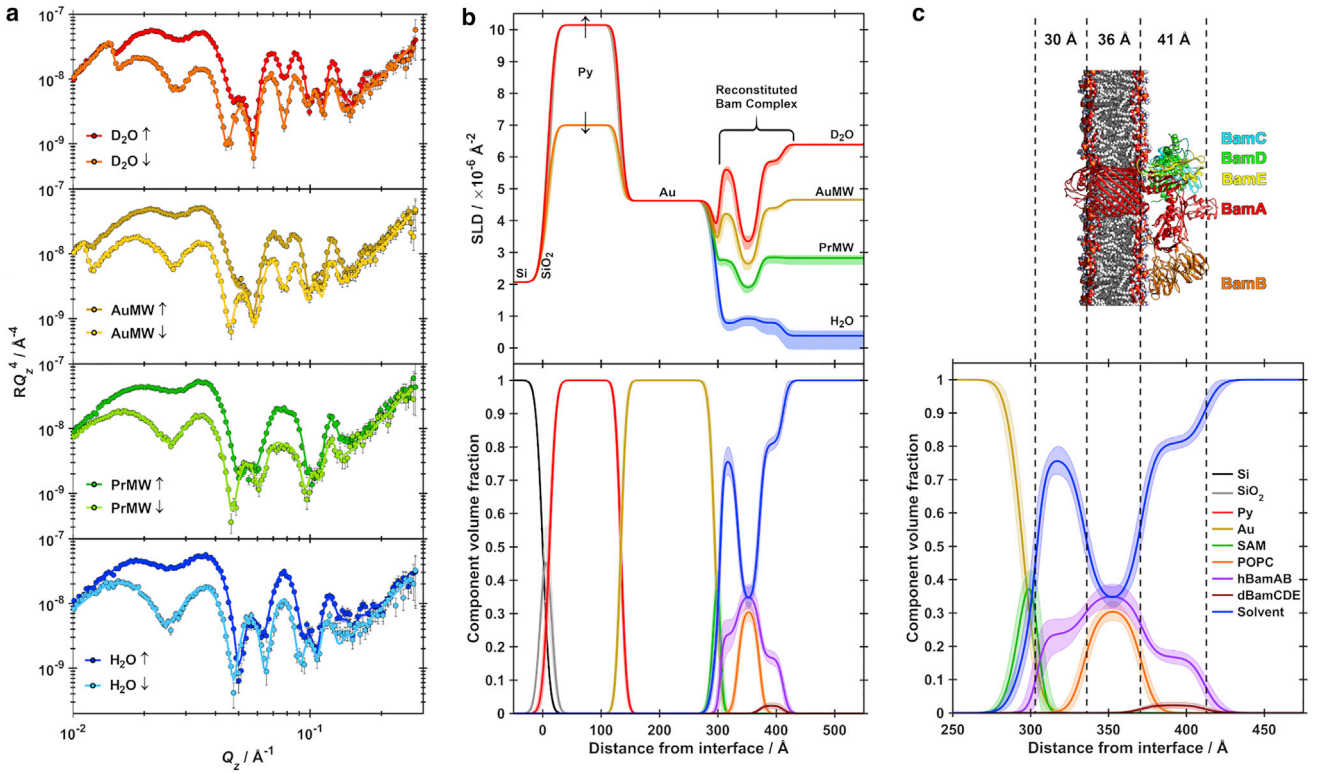

FIGURE 4 (*a*) PNR data (*points*) and fits (*lines*) for a hBamA$^{(L7H9)}$BdCDE:POPC membrane adsorbed to a DTSP-ANTA-Cu^{2+} functionalized gold surface, characterized in both spin-up (↑) and spin-down (↓) magnetic contrasts in D_2O (*red data*), Gold-matched water (*gold data*), PrMW (*green data*) and H_2O (*blue data*) solution isotopic contrasts. (*b*) SLD profiles (*top panel*) and component volume fraction profile (*bottom panel*) corresponding to fits shown in (*a*). (*c*) Component volume fraction profile corresponding to fits shown in (*a*), describing the membrane-containing interfacial region. Shaded regions represent the 95% confidence intervals determined from MCMC resampling of fits to the experimental data. Vertical dashed lines show layer boundaries for the interfacial proteo-bilayer region, overlaid with a schematic representation of a high-resolution model of the BamABCDE complex (Protein Data Bank: 5LJO) situated within a POPC bilayer.

Surface-tethered reconstituted Bam complex is functional in OMP insertion into the membrane

Following detailed structural investigation of the interfacial structure of the reconstituted BamA$^{(L7H9)}$BCDE complex, we next sought to investigate the functionality of the interfacial assembly in OMP insertion into the bilayer using QCM-D. We chose to investigate the insertion of two prototypical OMPs: OmpT and Ptn. Both these proteins have been previously shown to be substrates of BamABCDE, and both contain a transmembrane β-barrel which is assembled within the membrane by the Bam complex, though the β-barrel of Ptn functions as an autotransporter domain to fold, secrete, and finally cleave a large β-helix domain.

To insert OMPs from the periplasm into the OM, a chaperone is required to stabilize the unfolded nascent OMP (53). SurA is the primary chaperone involved in this process and is responsible for stabilizing the OMP during transit through the periplasm from the Sec machinery to the Bam complex (53). Initially, the interaction of SurA with either Ptn or OmpT was investigated with pure POPC solid-supported lipid bilayers (SLBs). Here, POPC bilayers were deposited on silicon substrates via the well-established vesicle fusion method. In all cases, frequency and dissipation responses were observed characteristic for vesicular adsorption and rupture. In the absence of BamA$^{(L7H9)}$BCDE, SurA alone (Fig. 5 *a*), or SurA prepared with either Ptn (Fig. 5 *a*) or OmpT (Fig. 5 *b*) leads to no persistent change in frequency or dissipation, indicating the lack of affinity of SurA with and without native OMPs for POPC bilayers alone. We subsequently investigated the interaction of SurA with the BamA$^{(L7H9)}$BCDE/POPC proteomembranes in the absence of unfolded OMPs (Fig. 5 *c*). A small decrease in frequency and increase in dissipation was observed in all cases, corresponding to an increase in adsorbed mass (Table 3). There are two possible explanations for this apparent minor adsorption. Firstly, incomplete coverage of the interfacial membrane could lead to bulk solvent-exposed DTSP-ANTA-Cu^{2+}, for which SurA may display some affinity despite lacking a His-tag. Alternatively, this adsorption could be due to specific interaction with the surface-tethered Bam complex. From viscoelastic modeling of QCM-D data (Figs. S7–S9; Table 3), we can estimate the surface excess of BamA$^{(L7H9)}$BCDE as 5.65 ± 1.01 pmol/cm^2. Upon interaction with SurA, we can estimate the adsorption of 6.94 ± 4.36 pmol/cm^2 of SurA, giving a ratio of SurA/Bam of 1.2 ± 0.7. Although

TABLE 2 Structural parameters obtained by fitting PNR data of hBamA(L7H9)BdCDE/POPC membrane tethered to an Si-Py-Au-DTSP-ANTA-Cu2 + substrate

Layer	Thickness (Å)	SLD ($\times 10^{-6}$ Å^{-2})		Component volume fractions (%)		Roughness (Å)
Si	ND	2.07[a]		Si:	100[a]	$9.5^{+0.5}_{-1.0}$
SiO_2	$11.3^{+2.6}_{-2.8}$	$3.59^{+0.26}_{-0.13}$		SiO_2:	100[a]	$9.2^{+0.6}_{-0.6}$
Permalloy	$122.5^{+0.5}_{-0.4}$	↑:	$10.15^{+0.01}_{-0.01}$	Permalloy:	100[a]	$7.7^{+0.3}_{-0.3}$
		↓:	$7.00^{+0.02}_{-0.01}$			
Gold	$161.1^{+0.5}_{-0.5}$	4.62[a]		Gold:	100[a]	$8.2^{+1.0}_{-1.0}$
DTSP-ANTA-Cu^{2+} SAM	$9.2^{+2.1}_{-2.1}$	1.80[a]		DTSP-ANTA-Cu^{2+}:	68^{+12}_{-9}[b]	$4.2^{+2.1}_{-1.1}$
				Solvent:	32^{+9}_{-12}	
hBamA$^{(L7H9)}$B (between SAM and membrane)	$30.5^{+4.1}_{-3.5}$	D_2O:	$3.09^{+1.43E-3}_{-2.57E-3}$	hBamA$^{(L7H9)}$B:	24^{+5}_{-5}[b]	$7.3^{+2.2}_{-2.4}$
		AuMW:	$2.77^{+0.45E-3}_{-0.66E-3}$			
		PrMW:	$2.45^{+0.02}_{-0.02}$	Solvent:	76^{+5}_{-5}	
		H_2O:	$2.01^{+0.03}_{-0.03}$			
hBamA$^{(L7H9)}$B + POPC bilayer	$36.3^{+3.2}_{-5.0}$	D_2O:	$1.77^{+0.13}_{-0.14}$	POPC:	31^{+5}_{-4}[b]	$7.3^{+2.2}_{-2.4}$
		AuMW:	$1.60^{+0.12}_{-0.12}$	hBamA$^{(L7H9)}$B:	35^{+4}_{-4}[b]	
		PrMW:	$1.43^{+0.10}_{-0.11}$	Solvent:	34^{+4}_{-6}	
		H_2O:	$1.20^{+0.09}_{-0.09}$			
hBamA$^{(L7H9)}$B dCDE (adjacent to bulk solvent)	$41.1^{+3.0}_{-2.8}$	D_2O:	$3.58^{+0.19}_{-0.19}$	hBamA$^{(L7H9)}$B:	17^{+2}_{-2}[b]	$7.3^{+2.2}_{-2.4}$
		AuMW:	$3.27^{+0.20}_{-0.19}$	dBamCDE	2^{+1}_{-1}	
		PrMW:	$2.95^{+0.20}_{-0.20}$	Solvent:	81^{+2}_{-2}	
		H_2O:	$2.52^{+0.21}_{-0.20}$			
Bulk solvent	ND	D_2O:	$6.39^{+0.01}_{-0.01}$	Solvent:	100[a]	ND
		AuMW:	$4.65^{+2.53E-3}_{-3.68E-3}$			
		PrMW:	$2.82^{+0.09}_{-0.09}$			
		H_2O:	$0.39^{+0.16}_{-0.17}$			

Error values indicate the 95% confidence intervals estimated from MCMC resampling.
ND, not determinable.
[a]Values were held constant throughout the fitting procedure.
[b]Values were not directly fit, but calculated from the fitted parameters and associated 95% confidence intervals calculated from MCMC chains of the dependent fitted parameters.

this value suggests near stoichiometric binding, this analysis likely overestimates the adsorbed mass due to contributions in the acoustic mass sensed by QCM-D from coupled solvent, and β-OG micelles in the case of BamA$^{(L7H9)}$BCDE, which is not fully accounted for despite viscoelastic modeling.

The introduction of SurA in the presence of either Ptn (Fig. 5 *d*) or OmpT (Fig. 5 *e*) to surface-tethered BamA$^{(L7H9)}$BCDE/POPC proteomembranes leads to substantially larger decreases in frequency and increases in dissipation compared to SurA alone (Table 3). This indicates the adsorption of a much larger mass, which persists after washing the surface in the same buffer. This is suggestive of the reconstituted Bam complex being functional in the folding and insertion of the OMPs into the planar membrane. Surface excesses estimated from viscoelastic modeling allows us to determine the molar ratio of Ptn/BamA$^{(L7H9)}$BCDE within the membranes as 2.8 ± 1.6 and OmpT/BamA$^{(L7H9)}$BCDE as 2.5 ± 0.7. These values are similar for both OMPs, suggesting the reconstituted Bam complex displays similar activity independent of the introduced OMP. Furthermore, these molar ratios suggest that the reconstituted Bam complex is functioning in an enzymatic fashion with a single Bam complex being able to insert multiple OMPs. Similar molar ratios observed for both Ptn and OmpT, despite the difference in molecular weights, suggest that the proximity of the Au-DTSP-ANTA-Cu^{2+} surface does not sterically hinder initial insertion into the membrane. This demonstrates the breadth of OMPs which are amenable for investigation using this platform.

While mass estimates from QCM-D experiments suggest that BamA$^{(L7H9)}$BCDE is able to enzymatically insert a variety of OMPs into the membrane, as mentioned above, mass estimates from QCM-D measurements are substantially influenced by coupled solvent, which viscoelastic modeling cannot fully account for. Recent cross-linking and structural studies have shown the existence of an intermediate folding step during OMP insertion in which the final β strand of the client β-barrel is bound to BamA β1, which remains bound until the OMP is fully folded (10,15,54). The proximity of the functionalized gold surface could therefore lead to a stalled Bam-substrate complex should the OMP not have sufficient space to fold any peripheral domains. To investigate the influence of surface proximity on OMP folding, we performed an in-situ OmpT activity assay (Fig. 5 *f*). Here, QCM-D experiments were performed where BamA$^{(L7H9)}$BCDE was reconstituted in POPC before interactions with SurA/OmpT (Fig. S10 *a*). Following this a 100 μM solution of a fluorogenic peptide (as described above) was recirculated over the sensor surface for 24 h. If OmpT is correctly folded and functional, the peptide will be cleaved by OmpT and an increase in fluorescence can be measured. The experiment was repeated using a POPC membrane without the Bam complex which was

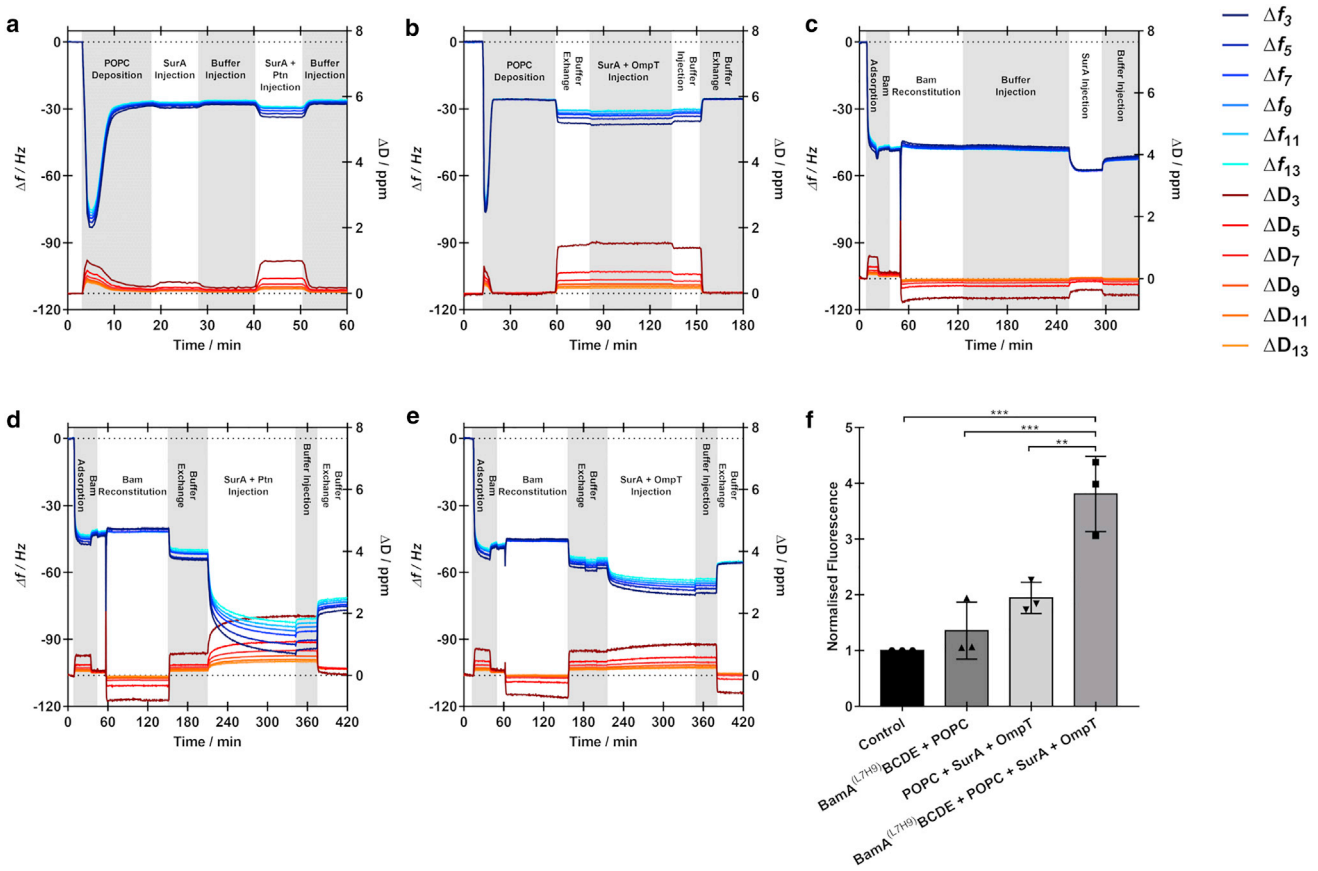

FIGURE 5 QCM-D data showing changes in frequency (*red-orange traces*) and dissipation (*blue traces*) corresponding to (*a*). The interaction of SurA before SurA and Ptn with a POPC SLB on a SiO_2 sensor. (*b*) The interaction of SurA and OmpT with a POPC SLB on a SiO_2 sensor. (*c*) The interaction of SurA with a BamA$^{(L7H9)}$BCDE/POPC proteomembrane assembled on a DTSP-ANTA-Cu^{2+} functionalized Au sensor. (*d*) The interaction of SurA and Ptn with a BamA$^{(L7H9)}$BCDE/POPC proteomembrane assembled on a DTSP-ANTA-Cu^{2+} functionalized Au sensor. (*e*) The interaction of SurA and OmpT with a BamA$^{(L7H9)}$BCDE/POPC proteomembrane assembled on a DTSP-ANTA-Cu^{2+} functionalized Au sensor. (*f*) Normalized changes in fluorescence following proteolytic cleavage of a self-quenching fluorogenic peptide recirculated over surface-tethered membranes containing POPC with and without BamA$^{(L7H9)}$BCDE, with and without interaction with SurA/OmpT. Points represent individual repeats, and error bars represent the standard deviation. Statistical significance is shown by double asterisks, indicating $p < 0.01$, and triple asterisk, indicating $p < 0.001$.

exposed to SurA/OmpT (Fig. S10 *c*), in addition to a BamA$^{(L7H9)}$BCDE-containing POPC membrane without any SurA/OmpT interaction (Fig. S10 *b*). These data show a significant increase in fluorescence over the control measurement (in which the peptide solution was not injected into the flow cells) and was only obtained in the complete system containing BamA$^{(L7H9)}$BCDE which has been incubated with SurA/OmpT. Crucially, there is also a significant increase in fluorescence over the samples lacking BamA$^{(L7H9)}$BCDE, indicating that OmpT is not being functionally inserted in the membrane in the absence on BamA$^{(L7H9)}$BCDE. These data demonstrate not only that the Bam complex is functional in catalyzing OmpT insertion, but also that OmpT is folded in a functional state. Despite this, there are undoubtedly steric restrictions associated with the proximity of the functionalized gold surface to the membrane, and some OMPs are expected to be too large to be folded in a functional state, though further investigation is required to understand the structural compatibility of inserted OMPs.

CONCLUSIONS

We have reported the development of a robust surface-based assay platform for investigating Bam-mediated OMP folding. Using a copper-chelating SAM adsorbed to a gold surface, we have been able to bind and reconstitute the complete Bam complex within a tethered phospholipid bilayer. Exploitation of both isotopic and magnetic-contrast variation allowed detailed structural characterization using PNR. This has provided, for the first time, structural information of the complete intact Bam complex within a planar phospholipid bilayer environment, consistent with high-resolution models of the surfactant-solubilized Bam complex. Crucially, using a Cu^{2+}-chelating SAM allows for orientational control of the Bam complex within the tethered membrane which is not feasible with alternative planar proteomembrane fabrication protocols, such as vesicular rupture.

In-situ assembly of the tethered proteomembrane, monitored with QCM-D, allowed for real-time monitoring of

TABLE 3 Frequency, dissipation and mass shifts observed during QCM-D measurements of the assembly and interactions of a BamABCDE/POPC membrane tethered to an Au-DTSP-ANTA-Cu^{2+} substrate

		Interaction		
Process	Parameter	SurA	SurA + Ptn	SurA + OmpT
BamABCDE/β-OG deposition	Δf3 (Hz)	−43.3 ± 4.2	−43.8 ± 2.2	−37.1 ± 10.5
	ΔD3 (ppm)	0.7 ± 0.2	0.7 ± 0.1	0.5 ± 0.4
	Δm (ng/cm^2)	1124.0 ± 201.8	1053.3 ± 67.7	957.9 ± 320.1
BamABCDE/POPC Reconstitution	Δf3 (Hz)	−4.9 ± 4.9	−4.9 ± 10.7	−8.6 ± 13.5
	ΔD3 (ppm)	−1.3 ± 1.1	−1.2 ± 1.7	−1.2 ± 1.4
	Δm (ng/cm^2)	−205.6 ± 129.9	96.7 ± 422.6	−15.3 ± 216.3
Chaperone ± OMP interaction	Δf3 (Hz)	−12.0 ± 6.2	−68.6 ± 40.6	−22.8 ± 7.6
	ΔD3 (ppm)	0.7 ± 0.6	5.4 ± 3.7	2.7 ± 0.7
	Δm (ng/cm^2)	308.2 ± 196.7	1358.4 ± 815.7	553.1 ± 560.3

All values are shown as the mean ± standard deviation of four independent measurements. Frequency and dissipation shifts are shown for the third harmonic (Δf3 and ΔD3, respectively) and changes in mass (Δm) are values estimated from viscoelastic modeling taking into account all harmonics measured. In the case of the initial adsorption of BamABCDE in β-OG micelles, values are given relative to the observed absolute frequency and dissipation values of DTSP-ANTA-Cu^{2+} functionalized substrates in β-OG buffer in the absence of BamABCDE. For subsequent processes, changes in frequency, dissipation and mass are given relative to that at the end of the previous process.

changes in mass and viscoelasticity during the assembly process, and demonstrated the activity of the reconstituted Bam complex in folding and inserting OMPs into the tethered membrane. Through viscoelastic modeling of QCM-D data, we were able to estimate the stoichiometries of proteinaceous components within the membrane. This allows a quantitative measurement of the activity of Bam in folding and inserting individual OMPs. The capability to measure the real-time activity of the Bam complex within a near native phospholipid bilayer provides a powerful platform for investigating and manipulating Bam-mediated OMP insertion.

Although now structurally well characterized, the precise mechanism of Bam-mediated OMP insertion remains speculative, as is the role of individual components of the Bam complex and the role of periplasmic chaperones in targeting OMPs destined for the OM to the Bam complex. The combination of structural and functional information available to be collected from the tethered membrane platform presented here has substantial application in answering these questions. Similarly, with increasing emergence of antimicrobial resistance, there is a substantial drive to disrupt the activity of the Bam complex as a strategy to compromise the integrity of the OM. The platform presented here is highly applicable to investigating both the structural and functional effect of novel antimicrobials on the Bam complex in a phospholipid bilayer in the absence of a detergent background.

SUPPORTING MATERIAL

Supporting material can be found online at https://doi.org/10.1016/j.bpj.2021.10.033.

AUTHOR CONTRIBUTIONS

S.C.L.H., L.A.C., M.J., and T.J.K. conceived the project. All authors were involved in the design of the experiments. S.C.L.H., L.A.C., P.S., D.J.H., P.W., J.W., J.W., N.G., C.S.L., C.H., G.W.H., M. J., and T.J.K. performed the experiments, while S.C.L.H., L.A.C., D.J.H., M.J., P.W., and T.J.K. analyzed the results. All authors reviewed the manuscript.

ACKNOWLEDGMENTS

We thank the Science and Technology Facilities Council and the ISIS Neutron & Muon Source for allocation of beamtime (RB1610262[55], RB1620475[56], RB17000777[57], and RB1800022[58]). We thank Professor Frank Heinrich and the NIST Nano-Fabrication Facility for the metal coatings used in the NR samples described in this study, C. Kinane for assistance on PolRef and D Kahne for the gift of pSK38, pSK46 plasmids.

This work was funded by the BBSRC through the following grants (TJK - BB/P0098401 and BB/S017283/1).

REFERENCES

1. Soufi, B., K. Krug, …, B. Macek. 2015. Characterization of the *E. coli* proteome and its modifications during growth and ethanol stress. *Front. Microbiol.* 6:103.
2. Li, G. W., D. Burkhardt, …, J. S. Weissman. 2014. Quantifying absolute protein synthesis rates reveals principles underlying allocation of cellular resources. *Cell.* 157:624–635.
3. Fàbrega, A., J. L. Rosner, …, J. Vila. 2012. SoxS-dependent coregulation of ompN and ydbK in a multidrug-resistant *Escherichia coli* strain. *FEMS Microbiol. Lett.* 332:61–67.
4. Prilipov, A., P. S. Phale, …, J. P. Rosenbusch. 1998. Identification and characterization of two quiescent porin genes, nmpC and ompN, in *Escherichia coli* BE. *J. Bacteriol.* 180:3388–3392.
5. Malinverni, J. C., J. Werner, …, T. J. Silhavy. 2006. YfiO stabilizes the YaeT complex and is essential for outer membrane protein assembly in *Escherichia coli*. *Mol. Microbiol.* 61:151–164.
6. Hart, E. M., and T. J. Silhavy. 2020. Functions of the BamBCDE lipoproteins revealed by bypass mutations in BamA. *J. Bacteriol.* 202:e00401-20.
7. Noinaj, N., S. E. Rollauer, and S. K. Buchanan. 2015. The β-barrel membrane protein insertase machinery from Gram-negative bacteria. *Curr. Opin. Struct. Biol.* 31:35–42.
8. Höhr, A. I. C., C. Lindau, …, N. Wiedemann. 2018. Membrane protein insertion through a mitochondrial β-barrel gate. *Science.* 359:eaah6834.
9. Schiffrin, B., D. J. Brockwell, and S. E. Radford. 2017. Outer membrane protein folding from an energy landscape perspective. *BMC Biol.* 15:123.

10. Doyle, M. T., and H. D. Bernstein. 2019. Bacterial outer membrane proteins assemble via asymmetric interactions with the BamA β-barrel. *Nat. Commun.* 10:3358.
11. Lee, J., D. Tomasek, …, D. Kahne. 2019. Formation of a β-barrel membrane protein is catalyzed by the interior surface of the assembly machine protein BamA. *eLife.* 8:e49787.
12. Gu, Y., H. Li, …, C. Dong. 2016. Structural basis of outer membrane protein insertion by the BAM complex. *Nature.* 531:64–69.
13. Jansen, K. B., S. L. Baker, and M. C. Sousa. 2015. Crystal structure of BamB bound to a periplasmic domain fragment of BamA, the central component of the β-barrel assembly machine. *J. Biol. Chem.* 290:2126–2136.
14. Iadanza, M. G., A. J. Higgins, …, N. A. Ranson. 2016. Lateral opening in the intact β-barrel assembly machinery captured by cryo-EM. *Nat. Commun.* 7:12865.
15. Tomasek, D., S. Rawson, …, D. Kahne. 2020. Structure of a nascent membrane protein as it folds on the BAM complex. *Nature.* 583:473–478.
16. Han, L., J. Zheng, …, Y. Huang. 2016. Structure of the BAM complex and its implications for biogenesis of outer-membrane proteins. *Nat. Struct. Mol. Biol.* 23:192–196.
17. Bergal, H. T., A. H. Hopkins, …, M. C. Sousa. 2016. The structure of a BamA-BamD fusion illuminates the architecture of the β-barrel assembly machine core. *Structure.* 24:243–251.
18. Bakelar, J., S. K. Buchanan, and N. Noinaj. 2016. The structure of the β-barrel assembly machinery complex. *Science.* 351:180–186.
19. Noinaj, N., A. J. Kuszak, …, S. K. Buchanan. 2013. Structural insight into the biogenesis of β-barrel membrane proteins. *Nature.* 501:385–390.
20. Gatzeva-Topalova, P. Z., T. A. Walton, and M. C. Sousa. 2008. Crystal structure of YaeT: conformational flexibility and substrate recognition. *Structure.* 16:1873–1881.
21. Kim, S., J. C. Malinverni, …, D. Kahne. 2007. Structure and function of an essential component of the outer membrane protein assembly machine. *Science.* 317:961–964.
22. Gatzeva-Topalova, P. Z., L. R. Warner, …, M. C. Sousa. 2010. Structure and flexibility of the complete periplasmic domain of BamA: the protein insertion machine of the outer membrane. *Structure.* 18:1492–1501.
23. Knowles, T. J., M. Jeeves, …, I. R. Henderson. 2008. Fold and function of polypeptide transport-associated domains responsible for delivering unfolded proteins to membranes. *Mol. Microbiol.* 68:1216–1227.
24. Sinnige, T., M. Weingarth, …, M. Baldus. 2015. Conformational plasticity of the POTRA 5 domain in the outer membrane protein assembly factor BamA. *Structure.* 23:1317–1324.
25. Warner, L. R., P. Z. Gatzeva-Topalova, …, M. C. Sousa. 2017. Flexibility in the periplasmic domain of BamA is important for function. *Structure.* 25:94–106.
26. Renault, M., M. P. Bos, …, M. Baldus. 2011. Solid-state NMR on a large multidomain integral membrane protein: the outer membrane protein assembly factor BamA. *J. Am. Chem. Soc.* 133:4175–4177.
27. Sinnige, T., K. Houben, …, M. Baldus. 2015. Insight into the conformational stability of membrane-embedded BamA using a combined solution and solid-state NMR approach. *J. Biomol. NMR.* 61:321–332.
28. Ward, R., M. Zoltner, …, D. G. Norman. 2009. The orientation of a tandem POTRA domain pair, of the beta-barrel assembly protein BamA, determined by PELDOR spectroscopy. *Structure.* 17:1187–1194.
29. Hughes, G. W., S. C. L. Hall, …, T. J. Knowles. 2019. Evidence for phospholipid export from the bacterial inner membrane by the Mla ABC transport system. *Nat. Microbiol.* 4:1692–1705.
30. Giess, F., M. G. Friedrich, …, W. Knoll. 2004. The protein-tethered lipid bilayer: a novel mimic of the biological membrane. *Biophys. J.* 87:3213–3220.
31. Richter, R., A. Mukhopadhyay, and A. Brisson. 2003. Pathways of lipid vesicle deposition on solid surfaces: a combined QCM-D and AFM study. *Biophys. J.* 85:3035–3047.
32. Hagan, C. L., S. Kim, and D. Kahne. 2010. Reconstitution of outer membrane protein assembly from purified components. *Science.* 328:890–892.
33. Reviakine, I., D. Johannsmann, and R. P. Richter. 2011. Hearing what you cannot see and visualizing what you hear: interpreting quartz crystal microbalance data from solvated interfaces. *Anal. Chem.* 83:8838–8848.
34. Webster, J., S. Holt, and R. Dalgliesh. 2006. INTER the chemical interfaces reflectometer on target station 2 at ISIS. *Physica B.* 385–386:1164–1166.
35. Clifton, L. A., S. C. L. Hall, …, J. H. Lakey. 2019. Structural investigations of protein-lipid complexes using neutron scattering. *Methods Mol. Biol.* 2003:201–251.
36. Heinrich, F., and M. Lösche. 2014. Zooming in on disordered systems: neutron reflection studies of proteins associated with fluid membranes. *Biochim. Biophys. Acta.* 1838:2341–2349.
37. Holt, S. A., A. P. Le Brun, …, J. H. Lakey. 2009. An ion-channel-containing model membrane: structural determination by magnetic contrast neutron reflectometry. *Soft Matter.* 5:2576–2586.
38. Hughes, A. V., S. A. Holt, …, J. H. Lakey. 2014. High coverage fluid-phase floating lipid bilayers supported by ω-thiolipid self-assembled monolayers. *J. R. Soc. Interface.* 11:20140245.
39. Abelès, F. 1948. Sur la propagation des ondes électromagnétiques dans les milieux stratifiés. *Ann. Phys.* 12:504–520.
40. Nelder, J. A., and R. Mead. 1965. A simplex method for function minimization. *Comput. J.* 7:308–313.
41. Sivia, D. S., and J. Skilling. 2006. Data Analysis: A Bayesian Tutorial, Second Edition. Oxford University Press, Oxford, UK.
42. Sivia, D. S., and J. R. P. Webster. 1998. The Bayesian approach to reflectivity data. *Physica B.* 248:327–337.
43. Tiberg, F., I. Harwigsson, and M. Malmsten. 2000. Formation of model lipid bilayers at the silica-water interface by co-adsorption with non-ionic dodecyl maltoside surfactant. *Eur. Biophys. J.* 29:196–203.
44. Shen, H. H., D. L. Leyton, …, T. Lithgow. 2014. Reconstitution of a nanomachine driving the assembly of proteins into bacterial outer membranes. *Nat. Commun.* 5:5078.
45. Horne, J. E., D. J. Brockwell, and S. E. Radford. 2020. Role of the lipid bilayer in outer membrane protein folding in Gram-negative bacteria. *J. Biol. Chem.* 295:10340–10367.
46. Jagalski, V., R. D. Barker, …, M. Cárdenas. 2015. Grafted biomembranes containing membrane proteins–the case of the leucine transporter. *Soft Matter.* 11:7707–7711.
47. Clifton, L. A., S. A. Holt, …, J. H. Lakey. 2015. An accurate in vitro model of the E. coli envelope. *Angew. Chem. Int. Ed. Engl.* 54:11952–11955.
48. Heinrich, F. 2016. Deuteration in biological neutron reflectometry. *Methods Enzymol.* 566:211–230.
49. Richter, R. P., R. Bérat, and A. R. Brisson. 2006. Formation of solid-supported lipid bilayers: an integrated view. *Langmuir.* 22:3497–3505.
50. Nakasako, M. 2004. Water-protein interactions from high-resolution protein crystallography. *Philos. Trans. R. Soc. Lond. B Biol. Sci.* 359:1191–1204, discussion 1204–1206.
51. Clifton, L. A., F. Ciesielski, …, J. H. Lakey. 2016. The effect of lipopolysaccharide core oligosaccharide size on the electrostatic binding of antimicrobial proteins to models of the Gram negative bacterial outer membrane. *Langmuir.* 32:3485–3494.
52. Ding, Y., T. Shiota, …, H. H. Shen. 2020. Characterization of BamA reconstituted into a solid-supported lipid bilayer as a platform for measuring dynamics during substrate protein assembly into the membrane. *Biochim. Biophys. Acta Biomembr.* 1862:183317.
53. Sklar, J. G., T. Wu, …, T. J. Silhavy. 2007. Defining the roles of the periplasmic chaperones SurA, Skp, and DegP in *Escherichia coli*. *Genes Dev.* 21:2473–2484.

54. Doyle, M. T., and H. D. Bernstein. 2021. BamA forms a translocation channel for polypeptide export across the bacterial outer membrane. *Mol. Cell.* 81:2000–2012.e3.

55. Hall, S. C. L., P. Sridhar, …, T. J. Knowles. 2016. The structure and orientation of the Bam complex in the Gram-negative outer membrane. STFC ISIS Neutron and Muon Source. https://doi.org/10.5286/ISIS.E.RB1610262.

56. Hall, S. C. L., P. J. Wotherspoon, …, T. J. Knowles. 2016. The mechanism of Bam mediated outer membrane protein folding. STFC ISIS Neutron and Muon Source. https://doi.org/10.5286/ISIS.E.RB1620475.

57. Hall, S. C. L., J. Wright, …, T. J. Knowles. 2017. The mechanism of Bam mediated outer membrane protein folding. STFC ISIS Neutron and Muon Source. https://doi.org/10.5286/ISIS.E.RB1700077.

58. Hall, S. C. L., C. S. Laxton, …, T. J. Knowles. 2017. The mechanism of Bam mediated outer membrane protein folding. STFC ISIS Neutron and Muon Source. https://doi.org/10.5286/ISIS.E.RB1800022.

Biophysical Journal, Volume *120*

Supplemental information

Surface-tethered planar membranes containing the β-barrel assembly machinery: a platform for investigating bacterial outer membrane protein folding

Stephen C.L. Hall, Luke A. Clifton, Pooja Sridhar, David J. Hardy, Peter Wotherspoon, Jack Wright, James Whitehouse, Nadisha Gamage, Claire S. Laxton, Caitlin Hatton, Gareth W. Hughes, Mark Jeeves, and Timothy J. Knowles

Supporting Information

Surface-Tethered Planar Membranes Containing the β-Barrel Assembly Machinery: A platform for Investigating Bacterial Outer Membrane Protein Folding

Stephen C. L. Hall[a], Luke A. Clifton[a] Pooja Sridhar[b], David J. Hardy[b], Jack Wright[d], James Whitehouse[d], Peter Wotherspoon[b], Nadisha Gamage[e], Claire S. Laxton[f], Caitlin Hatton[g], Gareth W. Hughes[b], Mark Jeeves[c], Timothy J. Knowles[b*]

[a]ISIS Pulsed Neutron and Muon Source, Science and Technology Facilities Council, Rutherford Appleton Laboratory, Didcot, Oxfordshire, OX11 OQX. U.K.

[b]School of Biosciences, University of Birmingham, Birmingham, B15 2TT, U.K.

[c]Institute of Cancer and Genomic Sciences, University of Birmingham, Birmingham, B15 2TT, U.K.

[d]Astbury Centre for Structural Molecular Biology, University of Leeds, LS2 9JT, U.K.

[e]Membrane Protein Laboratory, Diamond Light Source, Harwell Science & Innovation Campus, OX11 0DE, U.K.

[f] School of Life Sciences, University of Nottingham, NG7 2UH, U.K.

[g]School of Life Sciences, University of Warwick, CV4 7AL.

* To whom correspondence should be addressed:

Timothy J. Knowles

School of Biosciences, University of Birmingham, Birmingham, B15 2TT, U.K.

t.j.knowles@bham.ac.uk

Contents

Supplementary Experimental Section

Expression and Purification of hydrogenated BamA$^{(L7H9)}$B.

hBamA$^{(L7H9)}$B was expressed in *E. coli* strain C41(DE3) by growing the strain carrying pSK389H to OD_{600} = 0.4 at 37°C. The temperature was lowered to 18°C, once OD_{600}= 0.6 the cells were induced by addition of IPTG to a concentration of 1 mM. The cells were grown at this temperature for 16 hours and harvested by centrifugation at 6000 x g for 15 minutes at 4 °C. The pellets were re-suspended in 20 mM Tris pH 8, 100 mM NaCl and lysed by 3 passages through a continuous flow cell disruptor (Emulsiflex C3, Avestin). Debris and unlysed cells were removed by centrifugation at 10,000 x g for 10 minutes at 4 °C. The supernatant was then ultracentrifuged at 100,000 x g for 30 minutes at 4 °C to pellet membranes. These were either used immediately or frozen at -80 °C until required. Membranes were re-suspended by solubilisation in 50 mM Tris pH 8, 500 mM NaCl, 2% (w/v) DDM for 2 hours followed by ultra-centrifugation at 100,000 x g for 30 minutes at 4 °C to remove insoluble material. Ni-NTA affinity purification was performed by the addition of Ni-NTA agarose beads to the solution followed by gentle mixing at 4 °C overnight. The beads were loaded on to a disposable column and washed using 5 column volumes of 50 mM Tris pH 8, 500 mM NaCl, 10mM Imidazole, 0.1% (w/v) DDM then eluted in 0.5 mL fractions using 50 mM Tris pH 8, 500 mM NaCl, 250 mM Imidazole, 0.1% (w/v) DDM. The eluted fractions were tested for the presence of protein by SDS-PAGE. Those fractions containing protein were concentrated then further purified using size exclusion chromatography using a Superdex S200 16/60 PG column (GE Healthcare) using 50mM Tris pH 8, 150mM NaCl, 0.03% DDM buffer.

Expression of hydrogenated and deuterated forms of BamCD and assembly and purification of BamA$^{(L7H9)}$BCD.

BamCD was initially expressed in *E. coli* strain BL21(DE3) by growing the strain carrying the pSK46 plasmid in LB (to produce hBamCD) or M9 media in 100% D2O and supplemented with D-glucose (1,2,3,4,5,6,6-D7, 98%) (to produce dBamCD) at 37°C to an OD_{600}=0.4, lowering the temperature to 18°C and inducing with the addition of 1mM IPTG for 16 hours. Cells were harvested by centrifugation at 6000 x g for 15 minutes at 4 °C. The pellets were re-suspended in 20 mM Tris pH 8, 100 mM NaCl and lysed by 3 passages through a continuous flow cell disruptor (Emulsiflex C3, Avestin). Cell debris and unlysed cells were removed by centrifugation (75,000 x g, 30 minutes, 4°C) and the supernatant was filtered (0.2 µm PVDF syringe filter). Purified hBamA$^{(L7H9)}$B in 50 mM Tris pH 8, 150 mM NaCl, 0.03% DDM buffer was loaded on to a pre-equilibrated 5ml His-Trap column (GE Healthcare). Filtered supernatant containing either hBamCD or dBamCD was then loaded on to the column enabling in situ formation of either the hBamA$^{(L7H9)}$BCD or hBamA$^{(L7H9)}$BdCD complex. The column was washed using 5 column volumes of 50 mM Tris pH 8, 500 mM NaCl, 10 mM imidazole, 0.03% (w/v) DDM prior to elution in 0.5 mL fractions using 50 mM Tris pH 8, 500 mM NaCl, 250 mM Imidazole, 0.03% (w/v) DDM. Fractions containing BamA$^{(L7H9)}$BCD, as evidenced by SDS-PAGE, were concentrated then further purified using size exclusion chromatography using a Superdex S200 16/60 PG column (GE Healthcare) using 50 mM Tris pH 8, 150 mM NaCl, 0.03% DDM buffer.

Expression of hydrogenated and deuterated forms of BamE and assembly and purification of BamA$^{(L7H9)}$BCDE.

BamE was initially expressed in *E. coli* strain BL21(DE3) by growing the strain carrying the pET16b-BamE plasmid in LB (to produce hBamE) or M9 media in 100% D2O and supplemented with D-glucose (1,2,3,4,5,6,6-D7 98%) (to produce dBamE) at 37°C to an OD_{600}=0.4 then lowering the temperature to 18°C and inducing with the addition of 1 mM IPTG for 16 hours. Cells were harvested by centrifugation at 6000 x g for 15 minutes at 4 °C. The pellet was re-suspended in 20 mM Tris pH 8, 100 mM NaCl and lysed by 3 passages through a continuous flow cell disruptor (Emulsiflex C3, Avestin). Cell debris and unlysed cells were removed by centrifugation (75,000 x g, 30 minutes, 4°C). The supernatant was filtered using a 0.2 μm PVDF syringe filter and loaded on to a pre-equilibrated 5 mL His-Trap column (GE Healthcare). The column was washed with 5 column volumes of 50 mM Tris pH 8, 500 mM NaCl, 50 mM imidazole prior to elution in 0.5 mL fractions using 50 mM Tris pH 8, 500 mM NaCl, 250 mM Imidazole. Those fractions containing BamE, as evidenced by SDS-PAGE, were pooled and incubated with Factor Xa (GE Healthcare, 1 unit for every 100 μg of protein) and dialyzed into 50 mM Tris pH 8, 150 mM NaCl to remove the N-terminal hexa-histidine tag. The sample was further purified to remove the cleaved tag by repeat passage through a 5ml His-trap (GE Healthcare) column using the procedure listed above. Those fractions containing cleaved protein were pooled, concentrated, and further purified by size exclusion chromatography using a Superdex S75 26/60 PG column (GE Healthcare) using 50 mM Tris pH 8, 150 mM NaCl.

To produce hBamA$^{(L7H9)}$BCDE, hBamA$^{(L7H9)}$BCD was incubated with approximately 2-fold excess hBamE in 50 mM Tris pH 8, 150 mM NaCl, 0.03% DDM for 30 minutes prior to purification by size exclusion chromatography using a Superdex S200 16/60 PG column (GE Healthcare). To produce hBamA$^{(L7H9)}$BdCDE, hBamA$^{(L7H9)}$BdCD was incubated with dBamE in excess in 50mM Tris pH 8, 150mM NaCl, 0.03% DDM for 30 minutes prior to purification by size exclusion chromatography using a Superdex S200 16/60 PG column (GE Healthcare).

Expression and purification of SurA.

SurA was expressed and purified using the method of Iadanza et al. 2016 [1]. Plasmid pET-SurA was transformed in to *E. coli* (DE3) cells and grown in 4L of LB broth containing 50 μg/ml Kanamycin at 37°C with shaking (200rpm). At OD_{600}=0.4 the temperature was reduced to 18°C and left until OD_{600}=0.6. At this point the cells were induced with 1mM IPTG. After 16 hours the cells were harvested by centrifugation (6000 x g, 15 minutes, 4°C). Cells were re-suspended in 50 mM Tris pH 8, 500 mM NaCl, 50 mM imidazole, containing EDTA-free protease inhibitors (Roche) and lysed using a cell disruptor (Emulsiflex C3, Avestin). Cell debris and unlysed cells were removed by centrifugation (75,000 x g, 30 minutes, 4°C), the supernatant was filtered (0.2 μm PVDF syringe filter) and loaded on to a 5 mL HisTrap column (GE Healthcare). Washing was performed by passage of 5cv 50 mM Tris pH 8, 500 mM NaCl, 50 mM imidazole. His-tagged SurA was denatured on column using 50 mM Tris pH 8, 500 mM NaCl, 6 M guanidine-HCl and the protein eluted with a gradient of 50 mM Tris pH 8, 500 mM NaCl, 6 M guanidine and 500 mM imidazole. Protein containing fractions were assessed by SDS-PAGE then dialyzed against 50 mM Tris pH 8. His-tag removal was performed by incubation with thrombin (40-80 units depending on yield)

overnight at 4℃. Removal of un-cleaved His-SurA was performed by repeat passage through a 5 mL His-Trap column. Refolded-SurA was concentrated to 200 µM using Amicon Ultra (10 kDa MWCO) concentrators, aliquoted, then snap frozen in liquid nitrogen and stored at -80℃.

Expression and purification of OmpT.

pET-OmpT was transformed into *E. coli* (DE3) cells (NEB) and grown in 2 L of lysogeny broth (LB) medium containing 50 µg/ml kanamycin at 37℃ with shaking (200rpm). At OD_{600}=0.6 expression was induced by the addition of 1mM IPTG. After 4 hours the cells were harvested by centrifugation (6000 x g, 15 minutes, 4℃). Cells were re-suspended in 50 mM Tris pH 8 and lysed by three passages through a cell disrupter (C3 emulsiflex, Avestin). The insoluble fraction was collected by centrifugation (75,000 x g, 30 minutes, 4℃) and then resuspended in 50 mM Tris pH 8, 2% (v/v) Triton X-100 and incubated for 1 hour at room temperature. The insoluble fraction was pelleted by centrifugation (75,000 x g, 10 minutes, 4℃) and the pelleted material was then washed twice with 50 mM Tris pH 8, with centrifugation (75,000 x g, 10 minutes, 4℃) after each washing. The washed inclusion body was then solubilized in 50 mM Tris pH 8, 6 M guanidine HCl for 1 hour then centrifuged (75,000 x g, 30 minutes, 4℃) to remove insoluble material. The purity was assessed by SDS-PAGE. The supernatant was then filtered (0.2 µm PVDF syringe filter) and concentrated to 120 µM and snap frozen in liquid nitrogen and stored at -80℃.

Expression and purification of pertactin.

Plasmid pET26b expressing Pertactin (Genescript) was transformed into *E. coli* (DE3) cells (NEB) and grown in 2 L of lysogeny broth (LB) medium containing 50 µg/ml kanamycin at 37oC with shaking (200rpm). At OD_{600}=0.6 expression was induced by the addition of 1mM IPTG. After 4 hours the cells were harvested by centrifugation (6000 x g, 15 minutes, 4℃). Cells were re-suspended in 50 mM Tris pH 8, 150 mM NaCl and lysed by three passages through a cell disrupter (C3 emulsiflex, Avestin). The insoluble fraction was collected by centrifugation (75,000 x g, 30 minutes, 4℃) and then resuspended in 50 mM Tris pH 8, 2% (v/v) Triton X-100 and incubated for 1 hour at room temperature. The insoluble fraction was pelleted by centrifugation (35,000 x g, 10 minutes, 4℃) and the pelleted material was then washed twice with 50 mM Tris pH 8, with centrifugation (35,000 x g, 10 minutes, 4℃) after each washing. The washed inclusion body was then solubilized in 50 mM Tris pH 8, 8 M Urea for 1 hour and then centrifuged (75,000 x g, 30 minutes, 4℃) to remove insoluble material. The purity was assessed by SDS-PAGE. The supernatant was then filtered (0.2 µm PVDF syringe filter) and concentrated to 20 µM and snap frozen in liquid nitrogen and stored at -80℃.

Polarized Neutron Reflectometry Data Analysis

In modelling the interfacial structure, all experimental datasets were constrained against data collected for the Si-Py-Au-DTSP-ANTA-Cu^{2+} interface in D_2O, prior to the addition of β-OG solubilized BamABCDE. This interfacial structure was modelled as 5 layers between bulk Si and solvent, representing, SiO_2, permalloy, gold and the DTSP-ANTA-Cu^{2+} SAM. The scattering length density (SLD) of these layers were fixed according to known values (Table S1), with the exception of permalloy, where sputter coating can lead to a variable elemental composition and magnetic properties, resulting in slightly different nuclear and magnetic SLDs. The thickness and roughness was fit for

each of these layers, in addition to the hydration of the SAM, accounting for incomplete coverage and labile hydrogen exchange in different isotopic contrasts. These parameters were constrained across all experimental data sets collected on each substrate. Upon the addition of β-OG solubilized hBamA$^{(L7H9)}$BCDE in D_2O, three additional layers were included, representing a water gap containing extracellular loops of BamA which bind to the Cu^{2+}-SAM, a 'transmembrane' region composed of BamA and β-OG, and a final layer composed of periplasmic domains of each component of the Bam complex. The thickness and roughness of each of these layers was fit. Proteins contain labile hydrogens which exchange with the bulk solvent, which when the isotopic composition of the bulk solvent is changed, causes the SLD of the protein to be modified. The single SLD was calculated for Bam in each solvent (Table S1) and used throughout this analysis. The volume fraction of Bam (χ_{Bam}) was fit independently for each of these protein-containing layers, accounting for the intrinsic hydration of proteins in addition to incomplete coverage as a result of both binding density and the protein structure. This allows the SLD of peripheral membrane protein layers to be calculated as

$$SLD_{Peripheral\ Protein\ Layer} = \chi_{Bam}SLD_{Bam} + (1 - \chi_{Bam})SLD_{Solvent}$$

In the case of the central 'transmembrane' layer, the presence of β-OG would be expected to modify the SLD of this layer. The SLD of the transmembrane region was calculated from the fitted volume fraction of β-OG ($\chi_{\beta-OG}$) and the fitted volume fraction of Bam (χ_{Bam}), taking into account hydration as discussed above, as

$$SLD_{\beta-OG:Bam\ Layer} = \chi_{Bam}SLD_{Bam} + \chi_{\beta-OG}SLD_{\beta-OG} + (1 - (\chi_{Bam} + \chi_{\beta-OG}))SLD_{Solvent}$$

In modelling the interfacial structure after reconstitution of hBamA$^{(L7H9)}$BCDE within a POPC bilayer, we made the assumption that the structure of the complex remained unchanged, as did the volume fractions of protein in each layer. Therefore, the thickness and roughness of the three protein-containing layers was fit, constrained across datasets collected for adsorbed hBamABCDE in β-OG micelles. Similarly, as the volume fractions of protein in each layer was constrained across datasets collected for hBamABCDE:β-OG, the SLD of the peripheral protein layers remains unchanged by the addition of POPC. In the case of the transmembrane region, the formation of a hydrogenated POPC bilayer around the adsorbed Bam complex would be expected to cause a substantial difference in the SLD of this layer. A single SLD was calculated for POPC (Table S1), and the overall SLD of the transmembrane layer was calculated based on the fitted volume fraction of POPC (χ_{POPC}) and the constrained, fitted volume fraction of Bam (χ_{Bam}) as

$$SLD_{POPC:Bam\ Layer} = \chi_{Bam}SLD_{Bam} + \chi_{POPC}SLD_{POPC} + (1 - (\chi_{Bam} + \chi_{POPC}))SLD_{Solvent}$$

In modelling the interfacial structure of hBamA$^{(L7H9)}$BdCDE, the same approach was taken as with hBamA$^{(L7H9)}$BCDE, except the distribution of deuterated components throughout the protein-containing region was also taken into account. We did initially not make any *a priori* assumptions as to the location of the deuterated components, independently fitting for a volume fraction of dBamCDE in each of the three layers, so the average SLD of the Bam complex within each layer can be calculated as

$$SLD_{Bam\ (Average)} = \chi_{hBamAB}SLD_{hBamAB} + (1 - \chi_{hBamAB})SLD_{dBamCDE}$$

This strategy, however, was unable to provide a statistically significant distribution of dBamCDE throughout the interfacial assembly. We therefore constrained the model to allow dBamCDE presence only in the peripheral protein layer adjacent to the bulk solvent, consistent with both the known structures of the complete BamABCDE complex, and the orientational constraints imparted on the complex by the DTSP-ANTA-Cu^{2+} SAM.

Component volume fraction plots were generated from the MCMC chains of the fitted parameters using a custom MATLAB script, available upon request from the authors. Briefly, absolute volume fraction of all components throughout the interface were calculated (as described above) as a function of distance for each individual MCMC iteration on a layer-by-layer basis, using the 'asymconvstep' function included in RasCAL:

```
function asymconvstep (x,xw,xcen,s1,s2,h)
  %{
    x = vector of x values
    xw = Width of step function
    xcen = Centre point of step function
    s1 = Roughness parameter of left side
    s2 = Roughness parameter of right side
    h = Height of step function.
  %}
  r = xcen + (xw/2);
  l = xcen - (xw/2);

  a = (x-l)./((2^0.5)*s1);
  b = (x-r)./((2^0.5)*s2);

  f = (h/2)*(erf(a)-erf(b));
end
```

This function produces an error function with a width equal to the layer thickness, convoluted with different error functions on each side, with error function widths corresponding to interfacial roughnesses obtained for each layer. The height of the step function corresponds to the volume fraction of each component. Identical components in different layers were then summed together to create continuous distributions spanning multiple layers. Finally, the mean and 95% confidence intervals for the volume fraction of each component was calculated from all MCMC iterations as a function of distance from the Si interface.

Supplementary Data

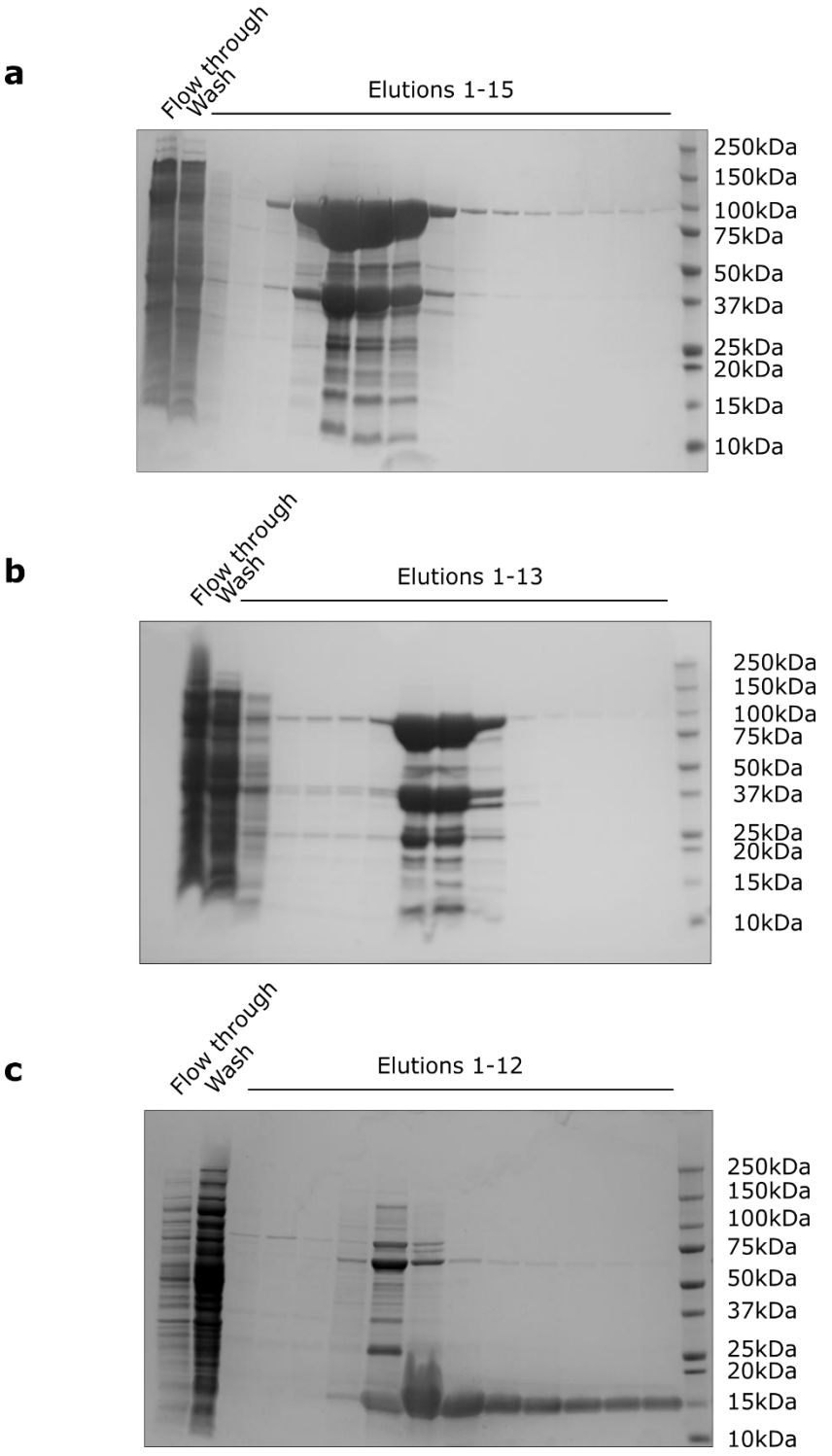

Figure S1 – hBamA$^{(L7H9)}$BCDE Ni-NTA purification. A) Ni-NTA purification of hBamA(L7H9)B over-expressed from *E. coli* strain C41(DE3). B) Ni-NTA purification of BamA(L7H9)B following incubation with detergent solubilized membranes derived from BL21(DE3) overexpressing hBamCD. C) Ni-NTA purification of hBamE over-expressed from *E. coli* BL21(DE3).

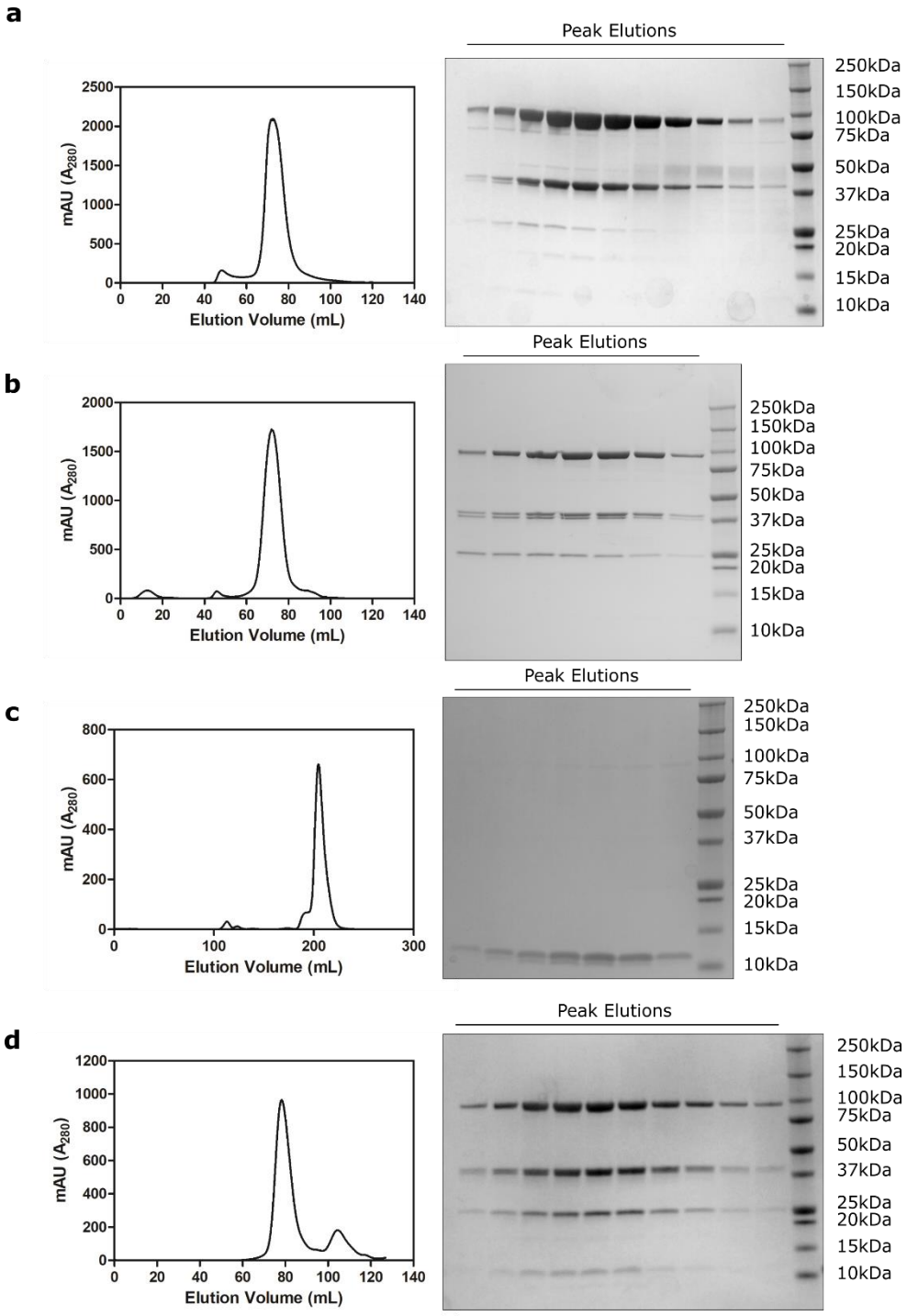

Figure S2 – hBamA$^{(L7H9)}$BCDE size exclusion chromatography purification. A) S200 16/60 Superdex (GE Lifesciences) size exclusion chromatogram of hBamA(L7H9)B (left) and subsequent SDS-PAGE of peak fractions (right). B) S200 16/60 Superdex (GE Lifesciences) size exclusion chromatogram of hBamA(L7H9)BCD (left) and subsequent SDS-PAGE of peak fractions (right). C) S75 26/60 Superdex (GE Lifesciences) size exclusion chromatogram of hBamE (left) and subsequent SDS-PAGE of peak fractions (right). D) S200 16/60 Superdex (GE Lifesciences) size exclusion chromatogram of hBamA(L7H9)BCDE (left) and subsequent SDS-PAGE of peak fractions (right).

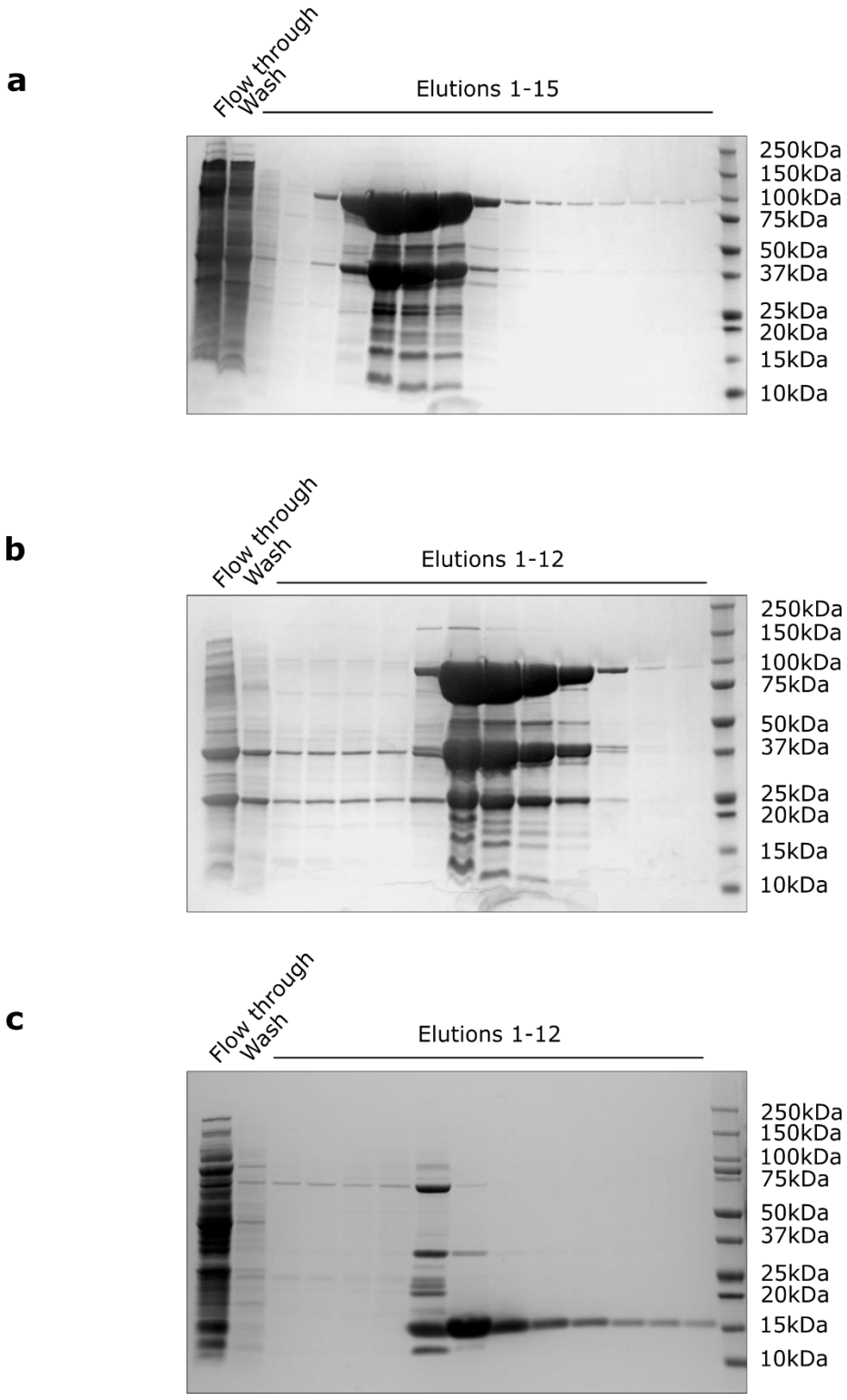

Figure S3 – hBamA$^{(L7H9)}$BdCDE Ni-NTA purification. A) Ni-NTA purification of hBamA(L7H9)B over-expressed from *E. coli* strain C41(DE3). B) Ni-NTA purification of BamA(L7H9)B following incubation with detergent solubilized membranes derived from BL21(DE3) overexpressing dBamCD in deuterated media. C) Ni-NTA purification of dBamE over-expressed from *E. coli* BL21(DE3) in deuterated media.

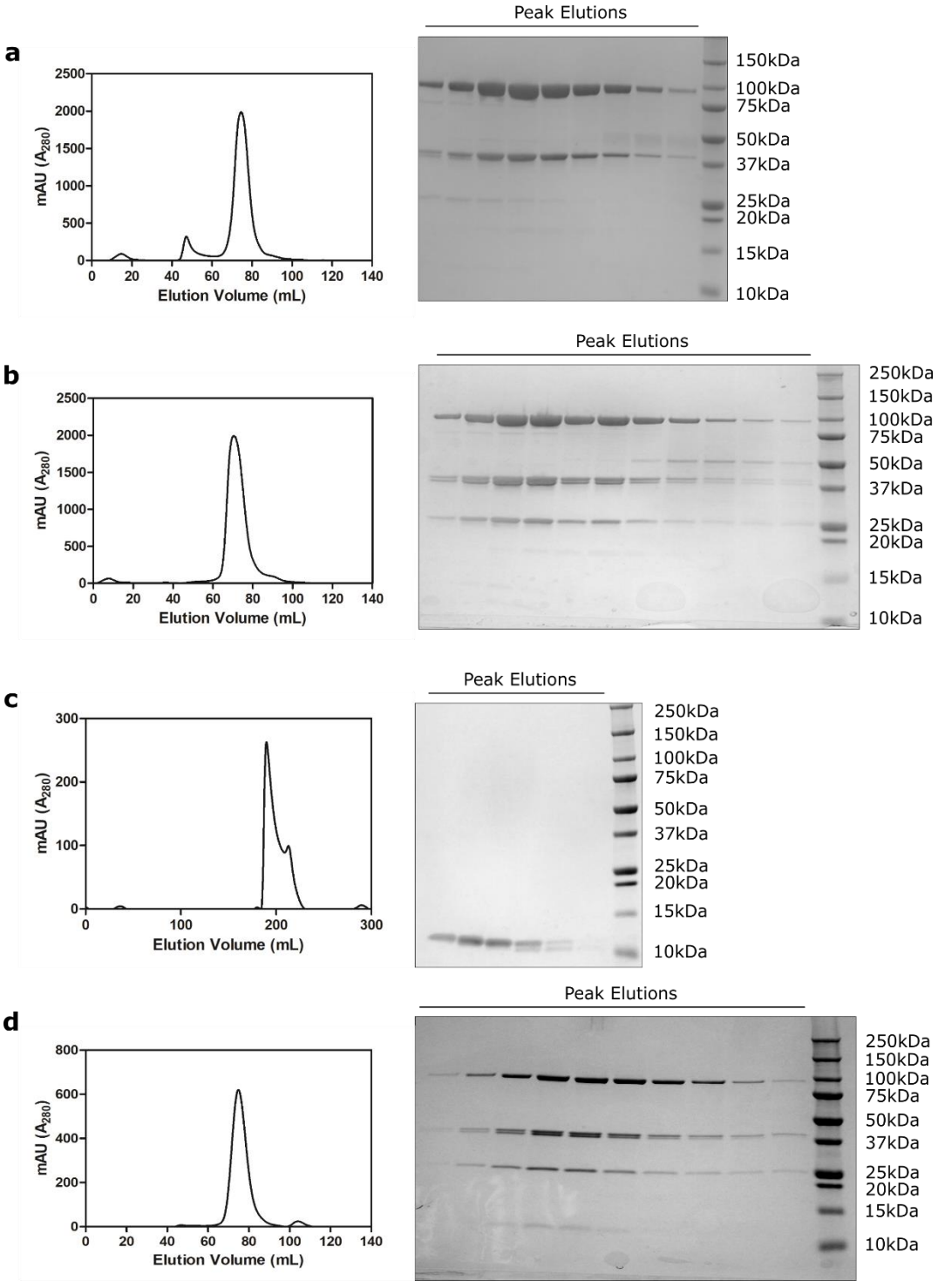

Figure S4 – hBamA$^{(L7H9)}$BdCDE size exclusion chromatography purification. A) S200 16/60 Superdex (GE Lifesciences) size exclusion chromatogram of hBamA(L7H9)B (left) and subsequent SDS-PAGE of peak fractions (right). B) S200 16/60 Superdex (GE Lifesciences) size exclusion chromatogram of hBamA(L7H9)BdCD (left) and subsequent SDS-PAGE of peak fractions (right). C) S75 26/60 Superdex (GE Lifesciences) size exclusion chromatogram of dBamE (left) and subsequent SDS-PAGE of peak fractions (right). D) S200 16/60 Superdex (GE Lifesciences) size exclusion chromatogram of hBamA(L7H9)BdCDE (left) and subsequent SDS-PAGE of peak fractions (right).

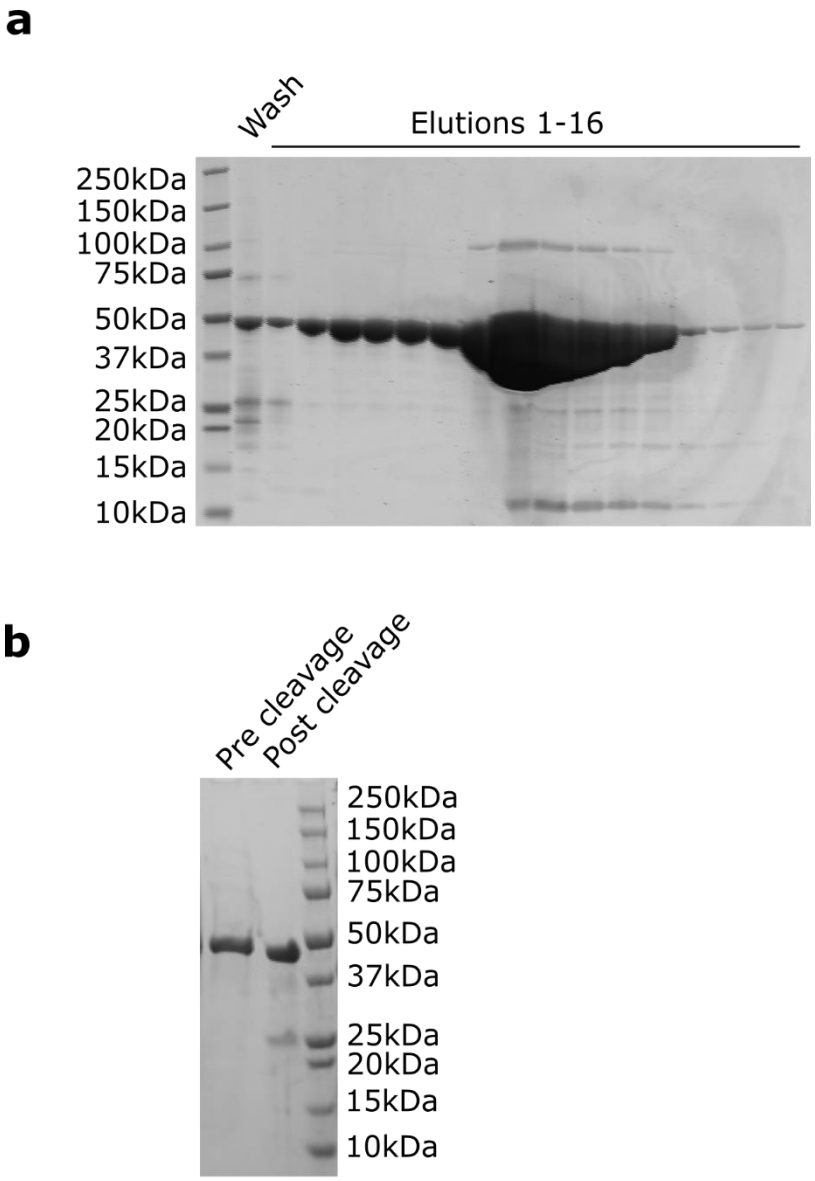

Figure S5 – Purification of SurA. A) SDS-PAGE of fractions following Ni-NTA purification of SurA under denaturing conditions in 6M guanidine hydrochloride. Fractions containing SurA were pooled, refolded by dialysis then subject to thrombin cleavage. B) SDS-PAGE following thrombin cleavage and cleanup using Ni-NTA purification showing pre and post cleavage purified samples.

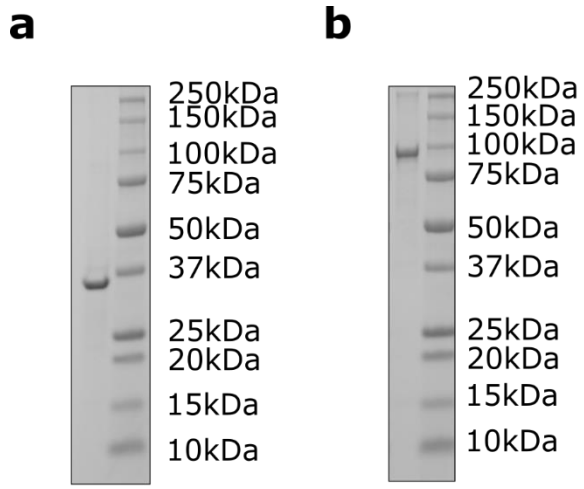

Figure S6 – OmpT & Pertactin inclusion body preparations. SDS-PAGE of A) OmpT and B) Pertactin inclusion body preparations following washing and resuspension in 6M guanidine HCl.

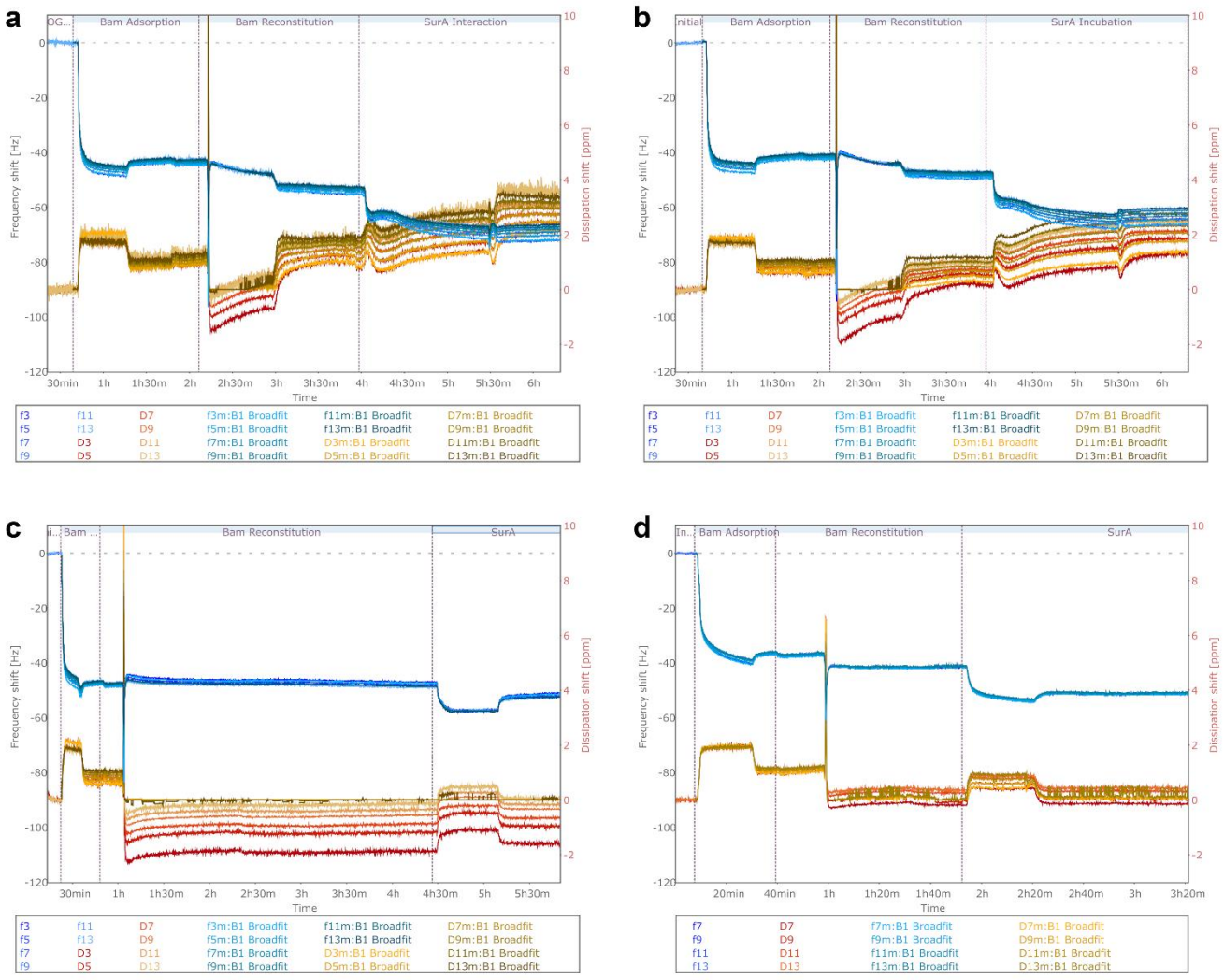

Figure S7. Raw QCMD Fits. Raw data and corresponding fits of 4 repeated QCM-D measurements (a-d.) measuring the interaction of SurA without any OMP with BamABCDE:POPC membranes adsorbed to gold substrates functionalized with DTSP-ANTA-Cu^{2+}

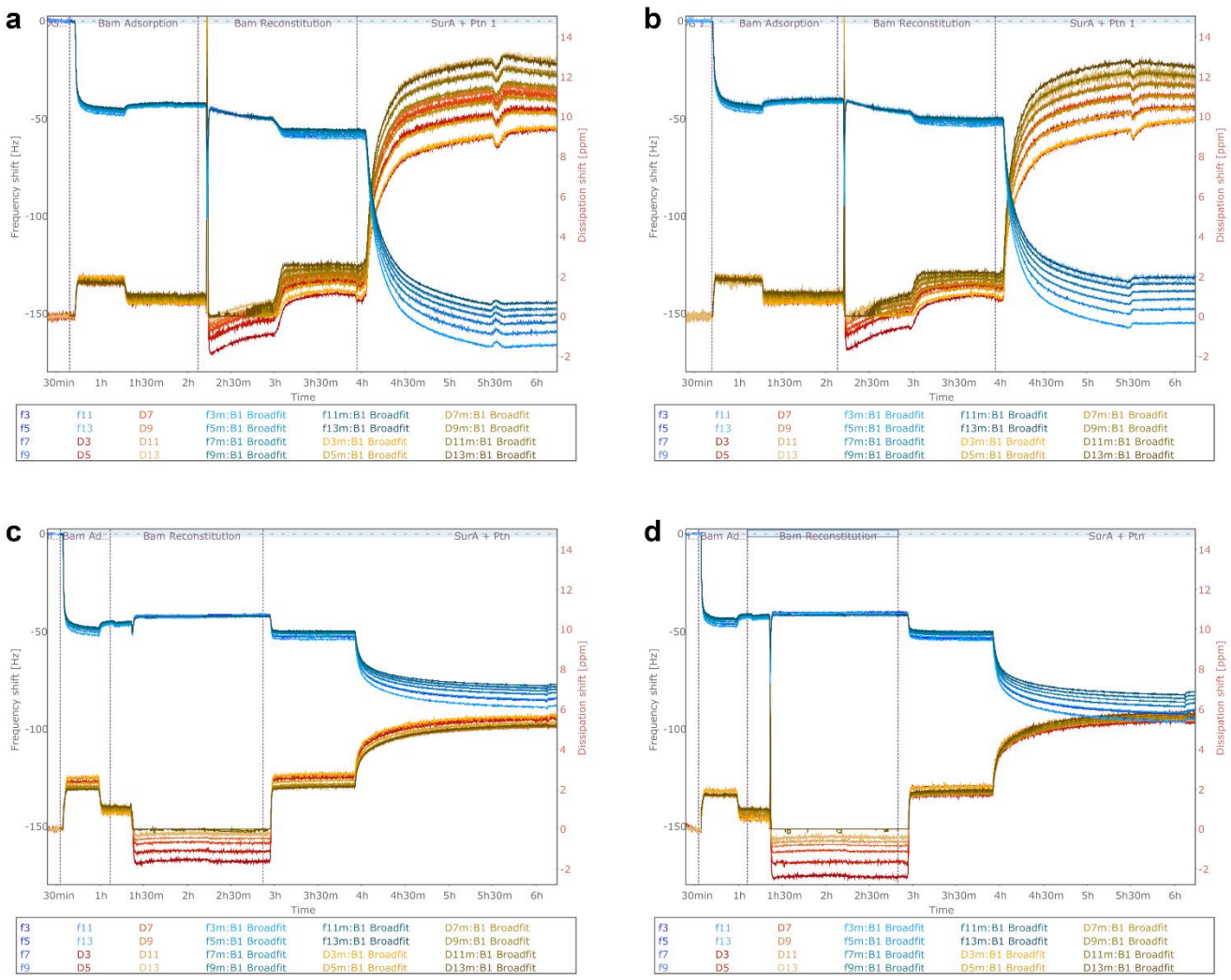

Figure S8. Raw QCMD Fits. Raw data and corresponding fits of 4 repeated QCM-D measurements (a-d.) measuring the interaction of SurA in the presence of pertactin with BamABCDE:POPC membranes adsorbed to gold substrates functionalized with DTSP-ANTA-Cu^{2+}

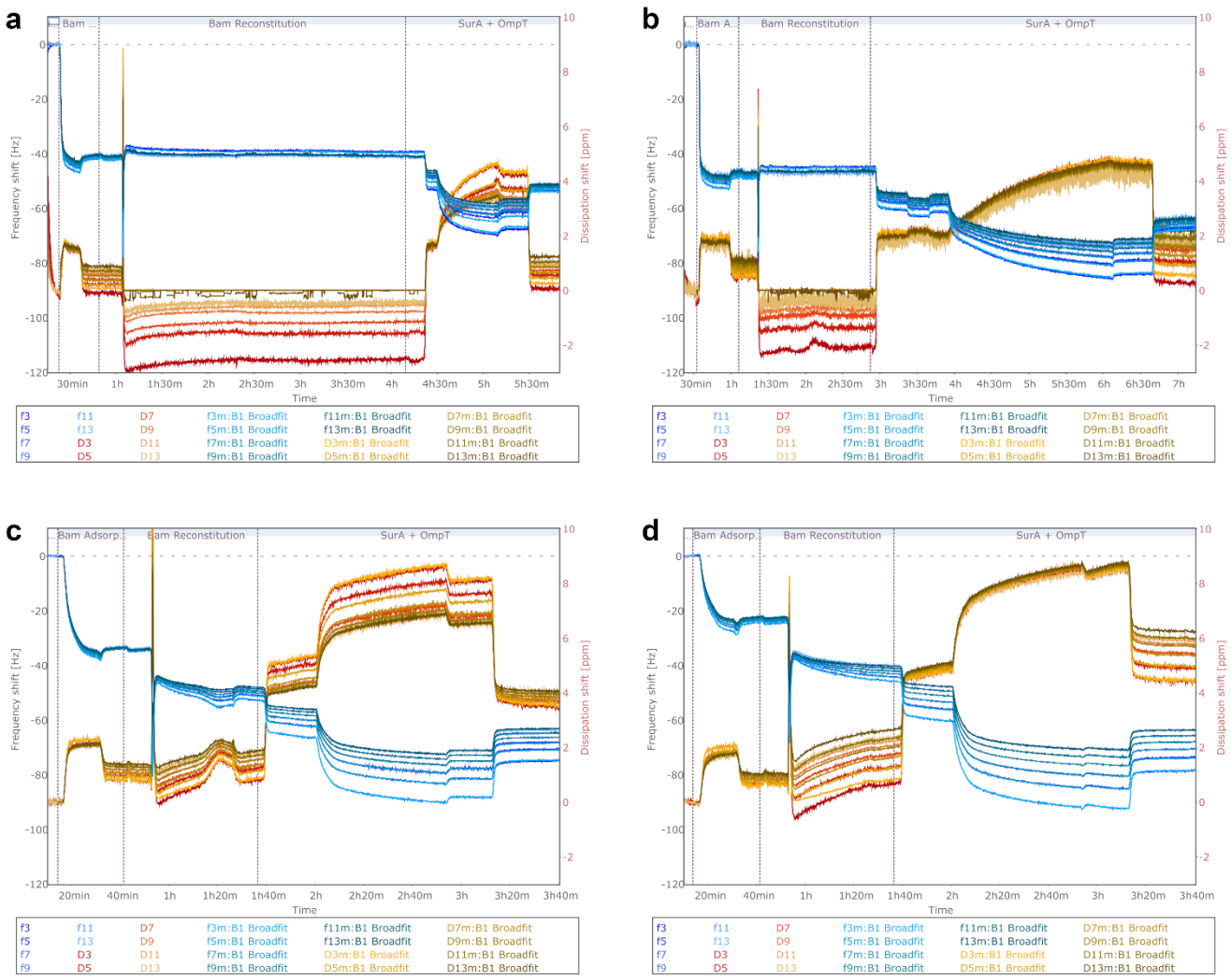

Figure S9. Raw QCMD Ftis. Raw data and corresponding fits of 4 repeated QCM-D measurements (a-d.) measuring the interaction of SurA in the presence of OmpTwith BamABCDE:POPC membranes adsorbed to gold substrates functionalized with DTSP-ANTA-Cu^{2+}

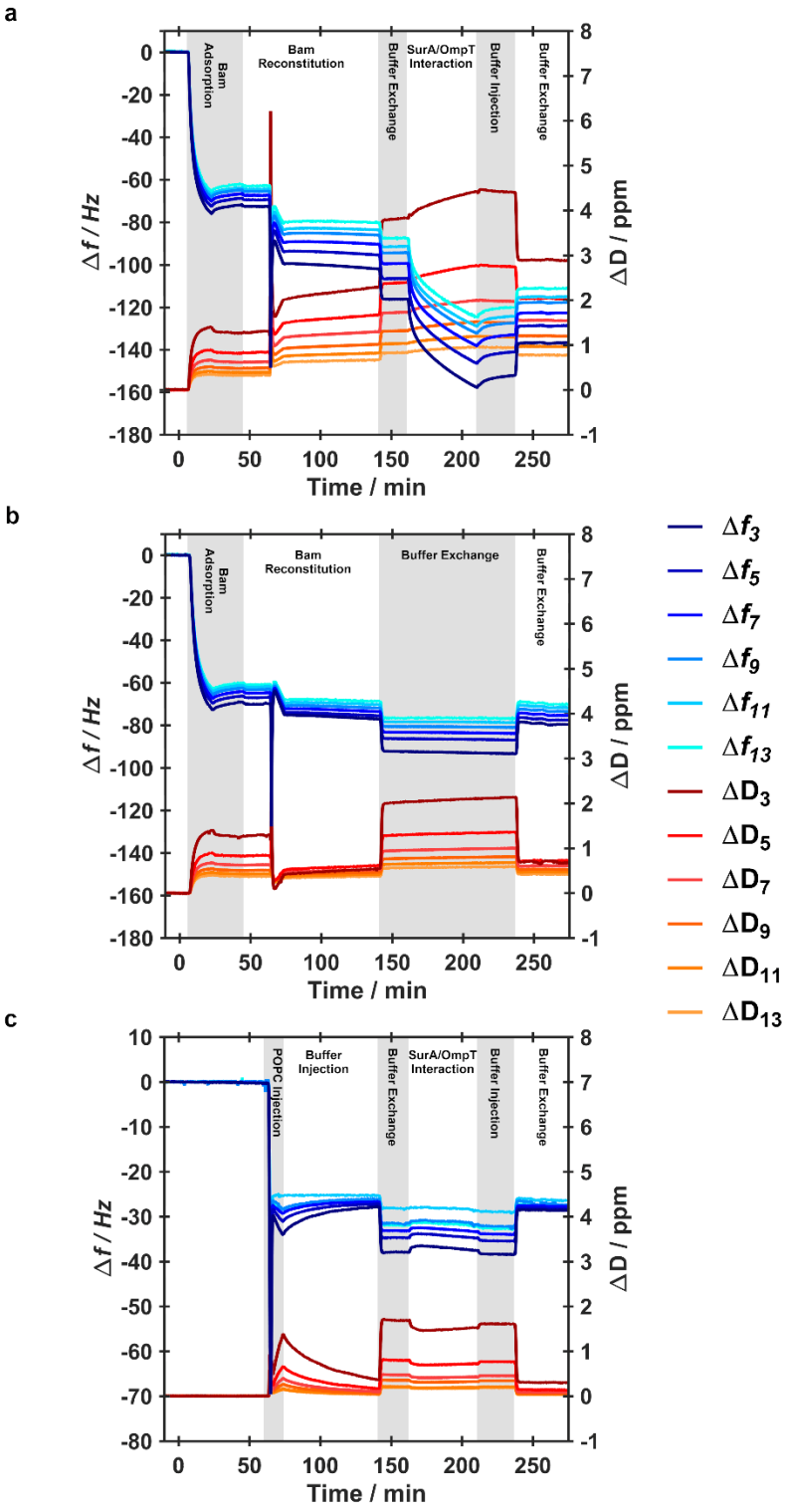

Figure S10. Representative QCM-D data obtained during surface assembly prior to *in-situ* OmpT Activity Assays. **a.** Assembly of BamA$^{(L7H9)}$BCDE:POPC membrane and subsequent interaction with SurA/OmpT. **b.** Assembly of a BamA$^{(L7H9)}$BCDE:POPC membrane without subsequent SurA/OmpT interaction. **c.** Assembly of a POPC membrane in the absence of BamA$^{(L7H9)}$BCDE, and subsequent interaction with SurA/OmpT.

Table S1. Known and calculated scattering length density values for components of the interfacial samples used in NR studies.

Sample Component	**SLD / $\times 10^{-6}$ Å^{-2}**
Silicon[1]	2.07
Silicon Oxide[1]	3.41
Gold	4.6
DTSP-ANTA	1.8
hBamABCDE (H_2O)	1.9
hBamABCDE (D_2O)	3.4
β-OG	1.5
POPC (total)	0.28
80% per d-Protein in H_2O	5.2
80% per d-Protein in D_2O	6.9
D_2O[1]	6.39
H_2O[1]	-0.56

Known SLD values taken from Stidder *et al* [2], Clifton *et al* [3] and Foglia *et al* [4]. Calculated SLD values for proteins were conducted using the protein SLD calculator (http://psldc.isis.rl.ac.uk/Psldc/) using the deuteration value obtained for the proteins by mass spectrometry analysis.

Supplementary References

1. Iadanza, M. G.; Higgins, A. J.; Schiffrin, B.; Calabrese, A. N.; Brockwell, D. J.; Ashcroft, A. E.; Radford, S. E.; Ranson, N. A., Lateral opening in the intact beta-barrel assembly machinery captured by cryo-EM. *Nature communications* **2016,** *7*, 12865.
2. Stidder, B.; Fragneto, G.; Roser, S. J., Effect of low amounts of cholesterol on the swelling behavior of floating bilayers. *Langmuir* **2005,** *21* (20), 9187-93.
3. Clifton, L. A.; Skoda, M. W.; Daulton, E. L.; Hughes, A. V.; Le Brun, A. P.; Lakey, J. H.; Holt, S. A., Asymmetric phospholipid: lipopolysaccharide bilayers; a Gram-negative bacterial outer membrane mimic. *J R Soc Interface* **2013,** *10* (89), 20130810.
4. Foglia, F.; Fragneto, G.; Clifton, L. A.; Lawrence, M. J.; Barlow, D. J., Interaction of amphotericin B with lipid monolayers. *Langmuir* **2014,** *30* (30), 9147-56.